Modeling blast waves, gas and particles dispersion in urban and hilly ground area

Sarah Hank*[1], Richard Saurel†[1,4], Olivier Le Metayer‡[2], and Emmanuel Lapébie§[3]

[1] RS2N, Bastidon de la Caou, 13360 Roquevaire, France
[2]Aix-Marseille Université, CNRS, IUSTI, UMR 7343 5 rue Enrico Fermi, 13013 Marseille, France
[3]CEA, DAM, GRAMAT, F-46500 Gramat, France
[4]University institute of France (IUF), 5 rue Enrico Fermi, 13453 Marseille, France

Abstract

The numerical simulation of waves propagation with fluid and particles dispersion in highly heterogeneous media such as cities, urban places, industrial plants and part of countries is addressed. Examples of phenomena under study are chemical gas products dispersion from damaged vessels, gas dispersion in urban places under explosion conditions, shock wave propagation in urban environment. A three-dimensional simulation multiphase flow code (HI2LO) is developed in this aim. To simplify the consideration of complex geometries, an heterogeneous discrete formulation is developed. When dealing with large scale domains, such as countries, the topography is considered with the help of elevation data. Meteorological conditions are also considered, in particular regarding complex temperature and wind profiles. Heat and mass transfers on sub-scale objects, such as buildings, trees and other obstacles are considered as well. Particles motion is addressed through a new turbulent model involving a single parameter to describe accurately plumes dispersion. Validations against experiments in basic situations are presented as well as examples of industrial and environmental computations.

1 Introduction and background

In many physical and industrial situations, it is important to predict the effects of blast wave, gas and particles dispersion resulting from an explosion. At least, two

*Sarah.Hank@polytech.univ-mrs.fr
†Richard.Saurel@polytech.univ-mrs.fr
‡Olivier.Lemetayer@polytech.univ-mrs.fr
§Emmanuel.Lapebie@cea.fr

types of difficulties appear when dealing with such numerical simulations. First, the topology of the medium under interest may be very complex regarding the presence of many obstacles or objects of different types. Second, large disparities in both space and time scales often require attention. This is the case when dealing with the dispersion of gases from explosions in strongly heterogeneous media such as urban places, cities and hilly grounds.
Various existing computational codes are available in this area: FLACS, developed for many years and widely documented [8,9,10,11,12], CFD-URBAN [13] or FEFLO [5,6,7]. These codes are used to predict gas clouds dispersion on complex geometries such as cities or industrial sites and allow the study of risk explosion effects. The approach promoted in the present work is similar to the one adopted in the FLACS code regarding topology and geometrical considerations. Indeed, FLACS takes into account the geometry details with the help of an internal porosity allowing the presence of obstacles within the control volume. FEFLO is an unstructured finite-element, finite volume code able to describe complex geometries with the help of sophisticated mesh generator. CFD-URBAN is able to model fluid flows and concentration dissemination in domains such as cities, but in the absence of shocks or blast effects.
Alternatively, many hydrocodes are available to model blast effects, such as AUTODYN [2], Air-3D [1] or SHAMRC [3]. These codes allow the study of unsteady phenomena such as shock waves in the presence of buildings, in the context of moderate geometrical complexity.
Thus, in the authors knowledge, there are mainly two existing strategies to consider both blast effects and gas dispersion in complex media:

- Flow solvers based on unstructured grids, such as FEFLO. Even if this approach is able to deal with heterogeneous media, small scale objects such as for example, trees or cars may cause difficulties.
- Cartesian grid solvers with an internal porosity, such as FLACS.

The present work belongs to the second class, with an heterogeneous media model built on the basis of rigorous mathematical basis. A discrete model [14] is developed to deal with gas dynamics in highly heterogeneous media. In addition, particles cloud dispersion effects are considered through a turbulent pressureless gas dynamics model fully coupled with the gas dynamics equations. In the present heterogeneous media, obstacles of very different sizes may be present. Large Eddy Simulation (LES) is no longer appropriate to solve the gas dynamics equations over such complex geometries, as the time to generate the mesh is prohibitive, as well as the computational time on long time scale events. Thus an homogenized model with cells of large dimensions containing obstacles is more appropriate [14]. This type of model belongs to the class of averaged multiphase flows models as described in [15,16] but with a single phase, the other phase corresponding to motionless obstacles. The model considers the volume occupied by the solid obstacles as well as their effects on the macroscopic flow dynamics. In this aim, the local pressure forces are determined by considering internal boundaries and specific Riemann solvers, or specific boundary solvers. In that sense, the method presented in this paper is quite close to embedded boundary methods (or cut-cell)

approaches [17,18] when dealing with the geoemtry description. It differs when very small obstacles are present, such as trees for which the exchange surface is not those of the cut-cell. We summarize in the present paper the discrete model of [14] and extend it to mass concentration determination as well as particle dynamics equations. In this aim, the high order ADER scheme [24,25] is used to reduce the numerical diffusion and compute accurately gas concentration fields. Mass diffusion and heat exchanges are introduced both at macroscopic and sub-scale levels. Last, examples of simulations on urban and on very large scales are presented to show capabilities of the three-dimensional simulation code.

2 Heterogeneous model building

To build the discrete model of heterogeneous media, a two phase control volume containing a gas and a motionless solid is considered. The equations for the dispersed phase (particles or droplets) will be considered later. The gas phase is governed by the multi-component Euler equations, dissipative effects being considered later as well.

2.1 Gas dynamics equations

The equations to consider in the gas phase are the multicomponent gas dynamics equations:

$$\frac{\partial \mathbf{U}}{\partial t} + \nabla.\mathbf{F} = 0 \tag{1}$$

Where $\mathbf{U}$ represents the conservative variables vector and $\mathbf{F}$ the fluxes vector:

$$\mathbf{U} = \Big(\rho Y_k, \rho, \rho\mathbf{u}, \rho E\Big)^T$$
$$\mathbf{F} = \Big(\rho Y_k\mathbf{u},\ \rho\mathbf{u},\ \rho\mathbf{u}\otimes\mathbf{u} + P\underline{\underline{\mathbb{I}}},\ (\rho E + P)\mathbf{u}\Big)^T$$

ρ, $\mathbf{u}$ and P represent respectively the mixture density, the velocity vector and the pressure. Y_k is the mass fraction of the chemical species k and E is the total energy, defined by

$$E = \frac{\|\mathbf{u}\|^2}{2} + e(T, Y_k)$$

The thermodynamic closure of System (1) is given by the ideal gas equation of state for the mixture:

$$e(T, Y_k) = \sum_{k=1}^{N} Y_k e_k(T)$$
$$e_k(T) = \int_{298}^{T} c_{v_k} dT + e_k^{298}$$

with $P = \rho RT$ and R, the mixture gas constant: $R = \dfrac{\hat{R}}{\hat{W}}$ with $\hat{W}$, the molar mass of the mixture ($\dfrac{1}{\hat{W}} = \displaystyle\sum_{k=1}^{N} \frac{Y_k}{W_k}$).

2.2 Integration on heterogeneous control volume

System (1) is integrated on a heterogeneous control volume containing both fluid and solid and over a time step (this control volume is shown in Figure 1). Space and time integration provide the discrete heterogeneous model. The procedure starts with,

$$\int_{t^n}^{t^{n+1}} \int_{V_i} \left\{ \frac{\partial \mathbf{U}}{\partial t} + \nabla.\mathbf{F} \right\} dV dt = 0$$

where V_i corresponds to the fluid volume within the cell, which is not necessarily equal to the cell volume, because of the possible presence of internal solid obstacles. The mass conservation equation is integrated hereafter, as a calculation example. The following integrals have to be computed,

$$\int_{t^n}^{t^{n+1}} \int_{V_i} \frac{\partial \rho}{\partial t} dV dt + \int_{t^n}^{t^{n+1}} \int_{S} \rho(\mathbf{u}.\mathbf{n}) dS dt = 0 \tag{2}$$

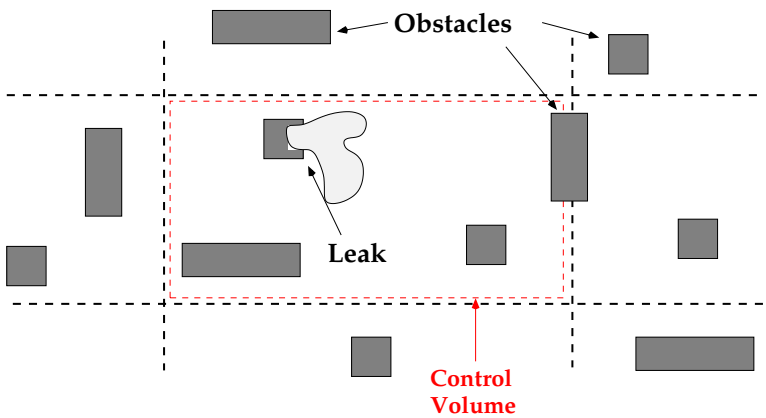

Figure 1: Representation of the heterogeneous control volume. Internal obstacles can potentially burst, inducing gases leakages within the cell.

Typical surfaces to consider are shown in Figure 2. $\mathbf{n}$ represents the outward normal vector for the fluid.

The integration surfaces can be fluid or solid. These surfaces are considered both inside and at the cell boundaries. With the definitions of Figure 2, it is possible to split the surface integral of Equation (2) in several parts,

$$S = S_F + S_S + S_F^0 + S_S^0$$

S_F and S_S are respectively, the fluid surface and the solid surface on the cell edges. S_F^0 and S_S^0 are respectively the permeable surface and the solid surface contained within the cell. Thus,

$$S_F^0 = S_{Fl}^{0x} + S_{Fr}^{0x} + S_{Fl}^{0y} + S_{Fr}^{0y} + S_{Fl}^{0z} + S_{Fr}^{0z}$$
$$S_S^0 = S_{Sl}^{0x} + S_{Sr}^{0x} + S_{Sl}^{0y} + S_{Sr}^{0y} + S_{Sl}^{0z} + S_{Sr}^{0z}$$

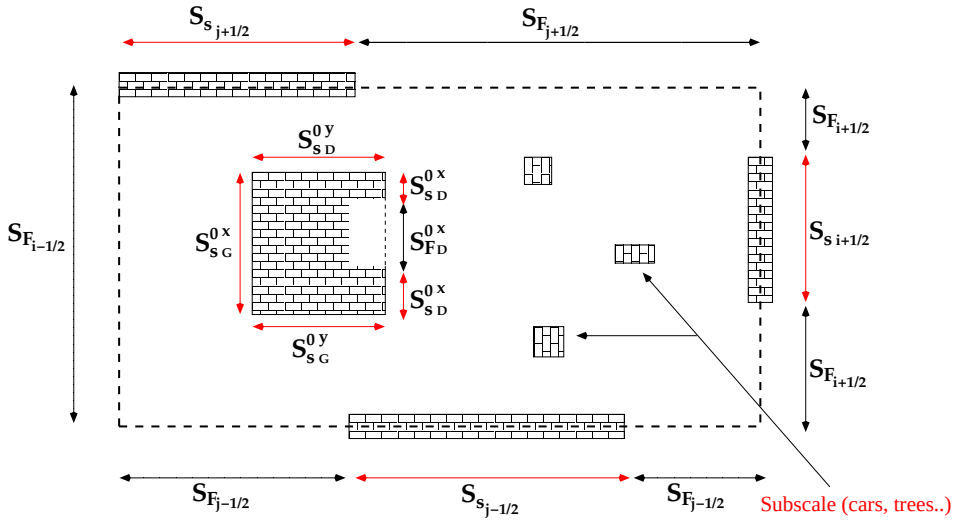

Figure 2: Representation of the integration surfaces which can be solid or fluid.

For the mass conservation equation, the flux contribution related to the solid surfaces vanishes. Regarding permeable surfaces at the cell edges, a conventional Riemann problem for the Euler equations [19] is solved to determine the fluxes. When dealing with internal obstacles, the same reasoning applies. Solid walls involve cancellation of the fluxes and tank boundary condition is used if the surface becomes permeable. Thus, the discrete model for the mass equation reads:

$$(\rho V)^{n+1}_{i,j,l} = (\rho V)^{n}_{i,j,l} - \Delta t \left\{ \begin{array}{c} \{(\rho u)^* S_F\}_{i+\frac{1}{2}} - \{(\rho u)^* S_F\}_{i-\frac{1}{2}} + \{(\rho v)^* S_F\}_{j+\frac{1}{2}} \\ - \{(\rho v)^* S_F\}_{j-\frac{1}{2}} + \{(\rho w)^* S_F\}_{k+\frac{1}{2}} - \{(\rho w)^* S_F\}_{k-\frac{1}{2}} \\ \boxed{\begin{array}{c} \sum \left[(\rho u)^* S^{0x}_{Fl} - (\rho u)^* S^{0x}_{Fr} + (\rho v)^* S^{0y}_{Fl} - (\rho v)^* S^{0y}_{Fr} \right] \\ + \sum \left[(\rho w)^* S^{0z}_{Fl} - (\rho w)^* S^{0z}_{Fr} \right] \end{array}} \end{array} \right\} \tag{3}$$

The variables marked with the superscript * correspond to the ones computed at a given cell boundary with the help of a Riemann solver (HLLC or exact solver) [19,20] . Equation (3) corresponds to a Godunov type scheme for heterogeneous cells. The fluxes linked to internal volumes are boxed in expression (3). The same calculation method is used for all the equations of System (1), in order to get the full discrete model. Integration of the energy equation gives a discrete formula, similar to the mass discrete equation. Some care has to be taken with the momentum equation. Indeed, additional terms due to the pressure force integration on internal obstacles surfaces are present. The resulting equation is given hereafter, the calculation details are given in [14].

$$
(\rho \mathbf{u} V)_{i,j,l}^{n+1} = (\rho \mathbf{u} V)_{i,j,l}^{n} - \Delta t \left(\begin{array}{c}
\left\{ \begin{array}{c}
\{(\rho u^2 + P)^* S_F\}_{i+\frac{1}{2}} - \{(\rho u^2 + P)^* S_F\}_{i-\frac{1}{2}} + (P_s^* S_S)_{i+\frac{1}{2}} \\
-(P_s^* S_S)_{i-\frac{1}{2}} + \{(\rho uv)^* S_F\}_{j+\frac{1}{2}} - \{(\rho uv)^* S_F\}_{j-\frac{1}{2}} \\
+\{(\rho uw)^* S_F\}_{k+\frac{1}{2}} - \{(\rho uw)^* S_F\}_{k-\frac{1}{2}} \\
\boxed{\begin{array}{c}
+\sum \left((\rho u^2 + P)^* S_{Fl}^{0x} - (\rho u^2 + P)^* S_{Fr}^{0x} + P_s^* S_{Sl}^{0x} - P_s^* S_{Sr}^{0x} \right) \\
+\sum \left((\rho uv)^* S_{Fl}^{0y} - (\rho uv)^* S_{Fr}^{0y} + (\rho uw)^* S_{Fl}^{0z} - (\rho uw)^* S_{Fr}^{0z} \right)
\end{array}}
\end{array} \right\} \mathbf{i} \\
\left\{ \begin{array}{c}
\{(\rho v^2 + P)^* S_F\}_{j+\frac{1}{2}} - \{(\rho v^2 + P)^* S_F\}_{j-\frac{1}{2}} + (P_s^* S_S)_{j+\frac{1}{2}} \\
-(P_s^* S_S)_{j-\frac{1}{2}} + \{(\rho uv)^* S_F\}_{i+\frac{1}{2}} - \{(\rho uv)^* S_F\}_{i-\frac{1}{2}} \\
+\{(\rho vw)^* S_F\}_{k+\frac{1}{2}} - \{(\rho vw)^* S_F\}_{k-\frac{1}{2}} \\
\boxed{\begin{array}{c}
+\sum \left((\rho v^2 + P)^* S_{Fl}^{0y} - (\rho v^2 + P)^* S_{Fr}^{0y} + P_s^* S_{Sl}^{0y} - P_s^* S_{Sr}^{0y} \right) \\
+\sum \left((\rho uv)^* S_{Fl}^{0x} - (\rho uv)^* S_{Fr}^{0x} + (\rho vw)^* S_{Fl}^{0z} - (\rho vw)^* S_{Fr}^{0z} \right)
\end{array}}
\end{array} \right\} \mathbf{j} \\
\left\{ \begin{array}{c}
\{(\rho w^2 + P)^* S_F\}_{k+\frac{1}{2}} - \{(\rho w^2 + P)^* S_F\}_{k-\frac{1}{2}} + (P_s^* S_S)_{k+\frac{1}{2}} \\
-(P_s^* S_S)_{l-\frac{1}{2}} + \{(\rho uw)^* S_F\}_{i+\frac{1}{2}} - \{(\rho uw)^* S_F\}_{i-\frac{1}{2}} \\
+\{(\rho vw)^* S_F\}_{j+\frac{1}{2}} - \{(\rho vw)^* S_F\}_{j-\frac{1}{2}} \\
\boxed{\begin{array}{c}
+\sum \left((\rho w^2 + P)^* S_{Fl}^{0z} - (\rho w^2 + P)^* S_{Fr}^{0z} + P_s^* S_{Sl}^{0z} - P_s^* S_{Sr}^{0z} \right) \\
+\sum \left((\rho uw)^* S_{Fl}^{0x} - (\rho uw)^* S_{Fr}^{0x} + (\rho vw)^* S_{Fl}^{0y} - (\rho vw)^* S_{Fr}^{0y} \right)
\end{array}}
\end{array} \right\} \mathbf{k}
\end{array} \right) .
$$

The resulting numerical scheme corresponds to a finite volume scheme (Godunov type scheme). This type of scheme has been successfully used for many flow conditions, ranging from high speed to atmospheric flows [4]. It is also possible to use approximate Riemann solvers with specific corrections allowing the convergence to the incompressible solution by modifying the wave speed within the solver when dealing with low Mach number (for details, see [36,37,38]. A second order space and time MUSCL-Hancock type extension [19] is used in the HI2LO code to solve the discrete heterogeneous model.

2.3 Discrete model of heterogeneous media validations:

Basic flow configurations are considered to assess the discrete heterogeneous model accuracy. Experimental data from different experiments are used in this aim.

2.3.1 Interaction of a shock wave with obstacles

The model is tested over some significant experimental flow configurations [21]. The interaction of a shock wave with solid plates inside a square cross section shock tube is considered. The experimental configuration is shown in Figure 3. Internal obstacles in the discrete formulation are used to model the vertical plates. It means that the internal obstacles are not considered at the cell boundaries but as internal source terms. Pressure gauges located at different places are considered to record pressure signal versus time.

Initial conditions in the high pressure chamber are the following, $P = 675kPa$

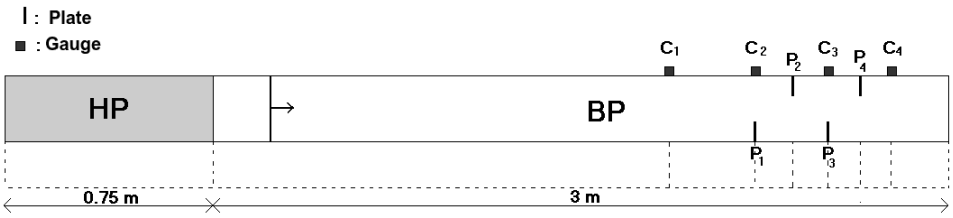

Figure 3: Experimental configuration of shock tube with vertical obstacles.

and $T = 338.6\ K$. Atmospheric conditions are considered in the low pressure chamber, $P = 101325\ Pa$ and $T = 296.49\ K$. The Mach number of the incident shock is M=1.5. Positions of the plates and gauges are:

$$x_{P_1} = 2.97m \quad x_{P_2} = 3.08m \quad x_{P_3} = 3.19m \quad x_{P_4} = 3.41m$$
$$x_{C_1} = 2.63m \quad x_{C_2} = 2.97m \quad x_{C_3} = 3.19m \quad x_{C_4} = 3.52m$$

750 cells in the **x** direction are used for the computations. Figure 4 shows

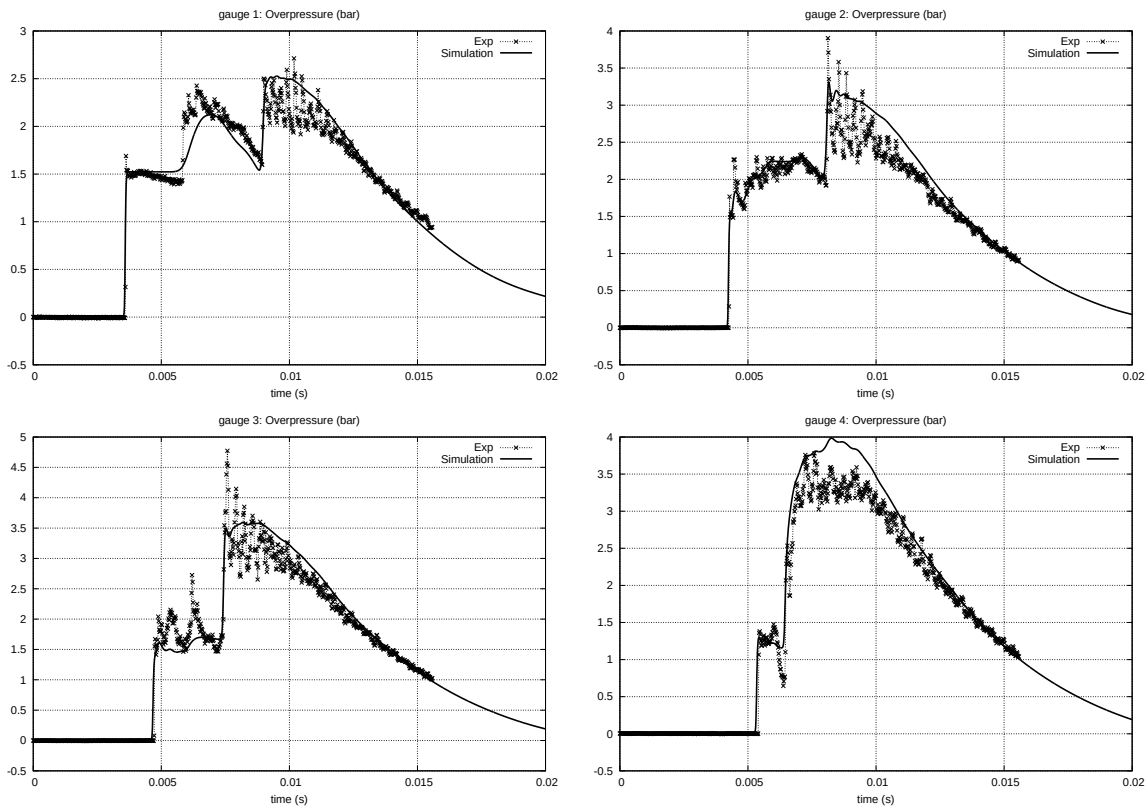

Figure 4: Pressure signals obtained with HI2LO (lines) compared to the experimental ones (symbols) at 4 different locations in the shock tube. The vertical obstacles have a surface equal to A/4 where A represent the shock tube cross section. The shock wave Mach number is 1.5.

the recorded and computed pressure signals at the various locations. Note that the computed pressure corresponds to an averaged value and not to a local pressure, such as the measured one. A Correct agreement is obtained, particularly regarding the waves dynamic that is well reproduced. The computed results are obtained with a coarse mesh, indeed, it involves 4 cells only in each cross section.

2.3.2 Blast wave interaction with a single obstacle

The interaction of a blast wave with a rectangular obstacle is addressed. The experiments were carried out in [22,23]. A small hemispherical charge made of propane-oxygen mixture is ignited and forms a detonation. A shock wave propagates in the air and interacts with the square obstacle. The pressure gauges positions and initial configuration are shown in the Figure 5.

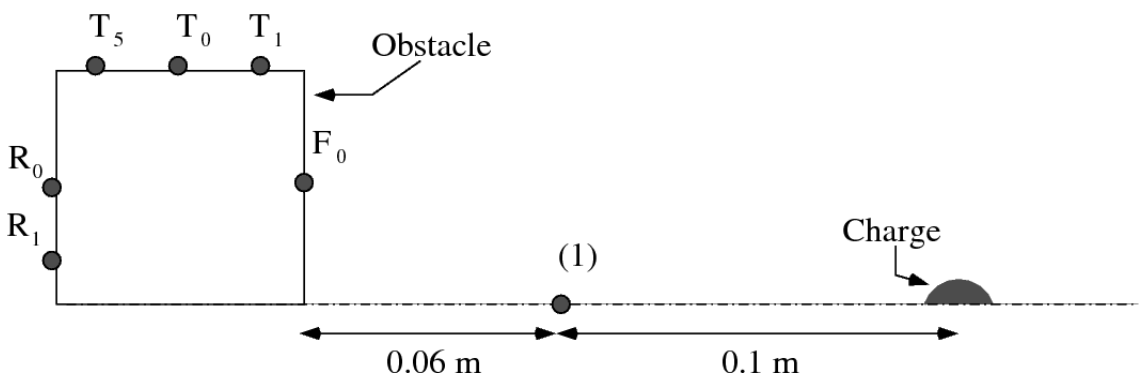

Figure 5: Experimental facilities and pressure sensor locations

The computations are performed in three dimensions with a mesh involving 2 millions cells. The propane-oxygen explosion is considered as a constant volume one, corresponding to the following conditions:

$$P_0 = 18.97\ 10^5 Pa, \qquad \rho_0 = 1.82\ kg/m^3,$$
$$\gamma = 1.206, \qquad C_v = 1385\ J/kg/K.$$

Atmospheric conditions are considered in the rest of the field. Results are shown in Figure 6 where the overpressure signals are plotted and compared to the experimental results. Correct agreement is obtained. The wave dynamics and overpressure peaks are well reproduced.

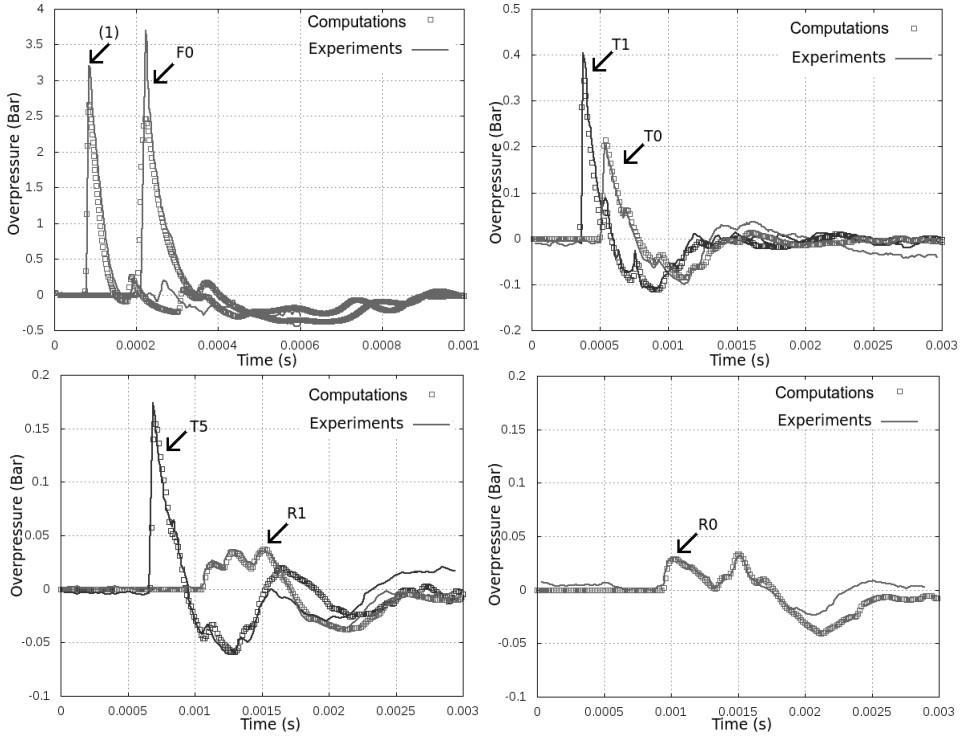

Figure 6: Pressure signals recorded at the various pressure sensors of the experiments (lines), compared to the numerical results (symbols).

3 A high order scheme to compute gas species concentration

The aim is now to track pollutant concentrations in the same type of heterogeneous media as previously. The present approach relying on finite volumes approximation in conjunction with long time evolutions results in numerical diffusion effects and forbids the correct prediction of the concentration fields. The solution considered here consists in using the third order version of the ADER scheme [24,25] for the gas species concentrations.

3.1 The ADER scheme

The ADER scheme allows the determination of a high-order flux which can be used in a finite volume Godunov type scheme. This scheme was introduced in [24,25] and is based on the resolution of the Generalized Riemann Problem (GRP) [19] and on the polynomial reconstruction of variables [26,27,28]. In the present approach, only the mass fraction equations are solved with the third order ADER scheme for simplicity reasons, such as numerical cost. Let us define the variable $q = \rho Y_k$. The generalized Riemann problem is defined

by the following Cauchy problem, in the one-dimensional case,

$$\begin{aligned} &\frac{\partial q}{\partial t} + \frac{\partial f(q)}{\partial x} = 0, \text{ with } f(q) = qu \\ &q(x,0) = \begin{cases} p_i(x), & x < 0 \\ p_{i+1}(x), & \text{otherwise} \end{cases} \end{aligned} \tag{4}$$

$p_i(x)$ and $p_{i+1}(x)$ are the Newton polynomials of order K respectively in cells i and $i+1$. In the conventional Godunov method, the variables are piecewise constant functions, while they are now piecewise polynomial functions.
The solution of the Cauchy problem (4) is given by the time Taylor series expansion:

$$q_{i+1/2}(\tau) = q(0,0^+) + \sum_{n=1}^{K} \frac{\partial^n q}{\partial t^n} \frac{\tau^n}{n!} \tag{5}$$

Where $q(0,0^+)$ denotes the solution of the conventional Riemann problem. The successive time derivatives have to be expressed in terms of the spatial derivatives with the help of Equation (4):

$$\begin{aligned} \frac{\partial q}{\partial t} + \frac{\partial f(q)}{\partial x} &= \frac{\partial q}{\partial t} + \frac{df(q)}{dq}\frac{\partial q}{\partial x} = 0, \\ \frac{\partial^2 q}{\partial t^2} + \frac{d^2 f(q)}{dq^2}\frac{\partial q}{\partial t}\frac{\partial q}{\partial x} &+ \frac{df(q)}{dq}\frac{\partial^2 q}{\partial t \partial x} = 0. \end{aligned}$$

Cross derivative appears in the second expression, and must be expressed. To do this, the spatial derivative of the first equation of system above is performed:

$$\frac{\partial^2 q}{\partial t \partial x} + \frac{d^2 f(q)}{dq^2}(\frac{\partial q}{\partial x})^2 + \frac{df(q)}{dq}\frac{\partial^2 q}{\partial x^2} = 0.$$

As $\frac{d^2 f(q)}{dq^2} = 0$, simplifications appear and finally the time derivatives can be expressed:

$$\begin{aligned} \frac{\partial q}{\partial t} &= -\frac{df(q)}{dq}\frac{\partial q}{\partial x}, \\ \frac{\partial^2 q}{\partial t^2} &= \left\{\frac{df(q)}{dq}\right\}^2 \frac{\partial^2 q}{\partial x^2}. \end{aligned}$$

These expressions are used in the time Taylor series expansion. However space derivatives must be evaluated at each cell boundary. Evolution equations are considered for their computations. The same equation is used for all the successive space derivatives, that is a version of Equation (4), with a frozen Jacobian.

$$\frac{\partial q_x^{(k)}}{\partial t} + \left(\frac{\partial f}{\partial q}\right)_0 \frac{\partial q_x^{(k)}}{\partial x} = 0. \tag{6}$$

where $q_x^{(k)}$ represents the kth spatial derivative and $\left(\frac{\partial f}{\partial q}\right)_0$ the frozen Jacobian, computed with the solution of the conventional Riemann problem. To

express the fluxes at the cell edges, several Riemann problems have to be solved, for the variable q and for its derivatives as shown in the Figure 7.

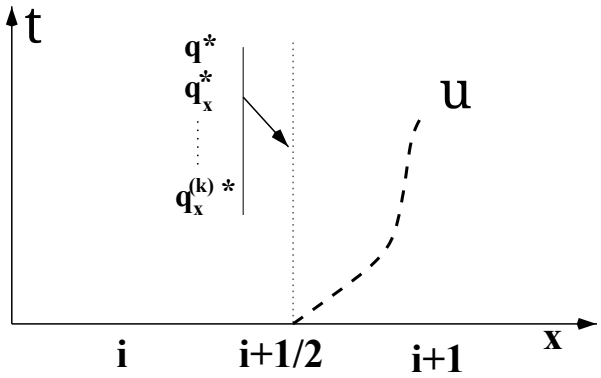

Figure 7: Structure of the solution of the generalized Riemann Problem in (x-t) plane.

After solving the Generalized Riemann Problem the fluxes are computed with (5). As shown latter, this scheme improves considerably transport equations solutions.

3.2 Algorithm summary and numerical examples

The ADER scheme can be summarized as follows:

- Compute the polynomial reconstruction of variables in each cell.
- Solve the conventional Riemann problem for the leading order solution.
- Solve the Riemann problem for spatial derivatives.
- Compute the flux time integral.

Results obtained with the third order ADER scheme are now compared with those obtained with others schemes on a basic test problem. It consists in the transport of a Gaussian profile at constant velocity. ADER computed results are compared to MUSCL-Hancock [19] ones.

The transport velocity is equal to 1 m/s and the mesh contains 100 cells. Periodic boundaries conditions are used in the computations. All the results are compared with the exact solution. Figure 8 shows the Gaussian function after 10 s of physical time. Figure 9 shows the results after 100 s. The MUSCL Hancock method tends to deform the Gaussian function while the third order ADER scheme conserves the correct shape.

These results clearly show that the ADER scheme is very accurate for the present application involving long time dispersion phenomena.

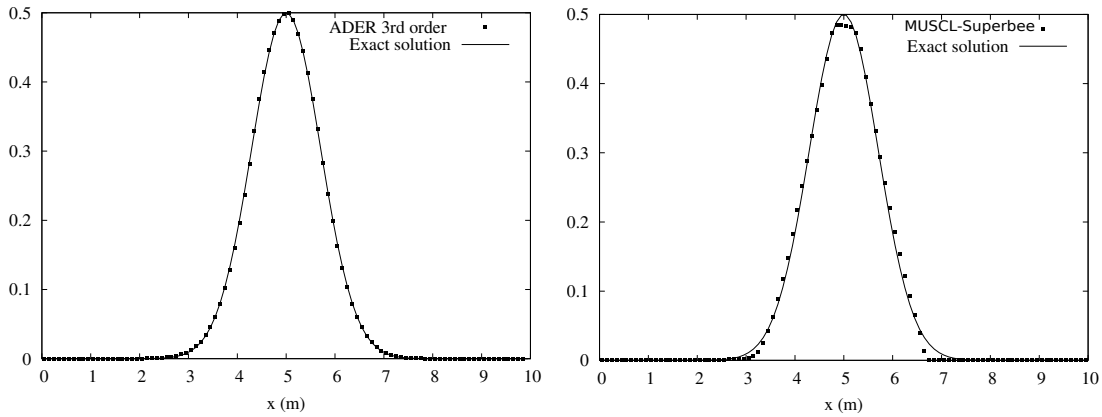

Figure 8: Gaussian profiles obtained with two different schemes (symbols) compared to the exact solution (lines) at time t =10 s.

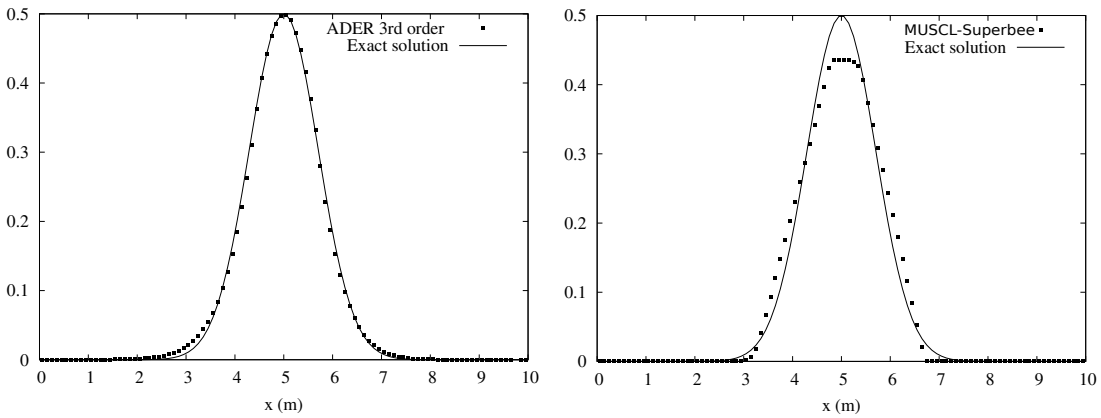

Figure 9: Gaussian profiles obtained with two different schemes (symbols) compared to the exact solution (lines) at time t =100 s.

4 Diffusion phenomena

As the gas species concentrations are now correctly computed, it is interesting to consider physical diffusion phenomena such as the molecular one, or the turbulent one, as well as heat diffusion. Details are given hereafter.

4.1 Mass diffusion

The formulation given in [29] is used, This formulation is generally associated to molecular diffusion, but it can be used to model turbulent diffusion. A diffusive flux appears in the mass fraction evolution equations implying an additional term in the total energy equation. Let us rewrite these two

equations as,

$$\frac{\partial \rho Y_k}{\partial t} + \nabla.\left(\rho \mathbf{u} Y_k + \mathbf{F_k}\right) = 0$$
$$, \frac{\partial \rho E}{\partial t} + \nabla.\left(\rho E \mathbf{u} + P\mathbf{u} + \mathbf{Q}\right) = 0.$$

With the following definitions,

$$\mathbf{F_k} = \sum_{l=1}^{N} C\mathbf{d_l}, \qquad \mathbf{d_l} = \frac{1}{P}\left\{\nabla P_l - Y_l \nabla P\right\}, \qquad \sum_{k=1}^{N} \mathbf{F_k} = 0,$$
$$\mathbf{Q} = \sum_{k=1}^{N} h_k \mathbf{F_k}, \qquad h_k = \frac{P_k}{\rho_k} + e_k(\rho_k, P_k).$$

C is a diffusion coefficient, Y_k is the mass fraction and P_k is the partial pressure of species k. With these definitions, it is possible to show that the system satisfies the entropy inequality.

$$\begin{aligned} \frac{\partial \rho s}{\partial t} + \nabla.\left(\rho \mathbf{u} s + \frac{Q}{T} - \sum_{k=1}^{N} \frac{g_k}{T}\mathbf{F}_k\right) &= \dot{s}, \\ \dot{s} = \frac{C}{PT}\sum_{k=1}^{N} \frac{1}{\rho_k}\left\{\left(\sum_{l=1,l\neq k}^{N} Y_l\right)\nabla P_k - Y_k\left(\sum_{l=1,l\neq k}^{N} \nabla P_l\right)\right\}^2 &\geq 0. \end{aligned} \tag{7}$$

These terms allow to model turbulent diffusion with an appropriate diffusive coefficient which can be evaluated using atmospheric stability consideration but also mass deposition on solid surfaces with the help of mass exchange coefficient at walls. Insertion of these dissipative terms in the discrete formulation of heterogeneous media is addressed hereafter in the frame of heat diffusion.

4.2 Heat transfer

To model heat transfer, conductive heat flux is added to the total energy evolution equation which become,

$$\frac{\partial \rho E}{\partial t} + \nabla.\left(\rho E \mathbf{u} + P\mathbf{u} + \mathbf{Q} + \mathbf{q}\right) = 0.$$

Where $\mathbf{q} = -\lambda \nabla T$ denotes the heat flux and λ the thermal conductivity of the gas mixture [52,53].

4.3 Integration of the diffusive terms

The heat and mass diffusion terms are integrated on the solid-gas control volume depicted in Figure 2. Diffusion fluxes appear at cell boundaries, as

well as exchange terms at the obstacles surfaces. Let us detail the calculations for the heat transfers, similar results being obtained for mass diffusion:

$$\Delta t \int_V \mathbf{q}_T \, dV = \Delta t \left(\begin{array}{c} \left\{ \{\mathbf{q}_T^{*f} S_f\}_{i+\frac{1}{2}} - \{\mathbf{q}_T^{*f} S_f\}_{i-\frac{1}{2}} + \{\mathbf{q}_T^{*s} S_s\}_{i+\frac{1}{2}} - \{\mathbf{q}_T^{*s} S_s\}_{i-\frac{1}{2}} \right\} .\mathbf{i} \\ + \left\{ \{\mathbf{q}_T^{*f} S_f\}_{j+\frac{1}{2}} - \{\mathbf{q}_T^{*f} S_f\}_{j-\frac{1}{2}} + \{\mathbf{q}_T^{*s} S_s\}_{j+\frac{1}{2}} - \{\mathbf{q}_T^{*s} S_s\}_{j-\frac{1}{2}} \right\} .\mathbf{j} \\ + \left\{ \{\mathbf{q}_T^{*f} S_f\}_{k+\frac{1}{2}} - \{\mathbf{q}_T^{*f} S_f\}_{k-\frac{1}{2}} + \{\mathbf{q}_T^{*s} S_s\}_{k+\frac{1}{2}} - \{\mathbf{q}_T^{*s} S_s\}_{k-\frac{1}{2}} \right\} .\mathbf{k} \\ \boxed{\begin{array}{c} + \sum \left\{ \mathbf{q}_T^{*f} S_{f,l}^{0x} - \mathbf{q}_T^{*f} S_{f,r}^{0x} + \mathbf{q}_T^{*s} S_{s,l}^{0x} - \mathbf{q}_T^{*s} S_{s,r}^{0x} \right\} .\mathbf{i} \\ + \sum \left\{ \mathbf{q}_T^{*f} S_{f,l}^{0y} - \mathbf{q}_T^{*f} S_{f,r}^{0y} + \mathbf{q}_T^{*s} S_{s,l}^{0y} - \mathbf{q}_T^{*s} S_{s,r}^{0y} \right\} .\mathbf{j} \\ + \sum \left\{ \mathbf{q}_T^{*f} S_{f,l}^{0z} - \mathbf{q}_T^{*f} S_{f,r}^{0z} + \mathbf{q}_T^{*s} S_{s,l}^{0z} - \mathbf{q}_T^{*s} S_{s,r}^{0z} \right\} .\mathbf{k} \end{array}} \end{array} \right) \tag{8}$$

The contribution of the internal obstacles is boxed in black in the previous expressions. Let us give some details on the expression of the fluxes q_T^*. When dealing with fluid surfaces S_f, the heat fluxes can be written as follow (in the $\mathbf{x}$ direction):

$$\mathbf{q}_T^* . \mathbf{i} = (q_T^*)_x = 2\lambda \frac{T_{i+1} - T^*}{\Delta x},$$

with T^* the temperature at the cell edge. Using of flux continuity conditions, we can write:

$$T^* = \frac{\lambda_i T_i + \lambda_{i+1} T_{i+1}}{\lambda_i + \lambda_{i+1}}$$

In the case of solid surfaces, or when dealing with internal obstacles, the heat fluxes is expressed with the help of an exchange coefficient h_c. For the sake of simplicity, the details are given for the flux in the $\mathbf{x}$ direction.

$$(q_T^*)_x \, S = h_c S (T_i - T_{wall})$$

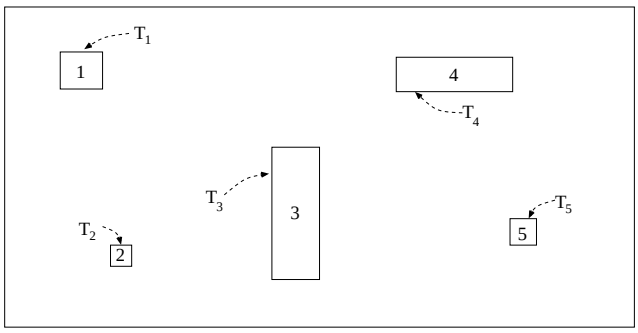

Figure 10: Schematization of a cell, containing different obstacles with their own temperatures.

Where S denotes the exchange surface of a given face obstacle and h_c the conductive heat exchange coefficient (see Appendix A). The heat fluxes have

to be summed up for all solid surfaces. Let S_{obst} denotes the total solid surface of an internal obstacle,

$$S_{obst} = S^{0x}_{s,l} + S^{0x}_{s,r} + S^{0y}_{s,l} + S^{0y}_{s,r} + S^{0z}_{s,l} + S^{0z}_{s,r}.$$

For a cell i, j, k containing N internal obstacles of different temperatures T_{wall} (see Figure 10), the total heat flux reads,

$$\sum_{l=1}^{N} h_c \left(S_{obst}\right)_l \left(T_{i,j,k} - (T_{wall})_l\right).$$

The discrete relation (8) now becomes,

$$\Delta t \int_V \mathbf{q}_T \, dV = \Delta t \left(\begin{array}{c} \left\{ \mathbf{q}_T^{*f} S_f \right\}_{i+\frac{1}{2}} - \left\{ \mathbf{q}_T^{*f} S_f \right\}_{i-\frac{1}{2}} + \left\{ \mathbf{q}_T^{*s} S_s \right\}_{i+\frac{1}{2}} - \left\{ \mathbf{q}_T^{*s} S_s \right\}_{i-\frac{1}{2}} + \sum \left\{ \mathbf{q}_T^{*f} S^{0x}_{f,l} - \mathbf{q}_T^{*f} S^{0x}_{f,r} \right\} . \mathbf{i} \\ + \left\{ \mathbf{q}_T^{*f} S_f \right\}_{j+\frac{1}{2}} - \left\{ \mathbf{q}_T^{*f} S_f \right\}_{j-\frac{1}{2}} + \left\{ \mathbf{q}_T^{*s} S_s \right\}_{j+\frac{1}{2}} - \left\{ \mathbf{q}_T^{*s} S_s \right\}_{j-\frac{1}{2}} + \sum \left\{ \mathbf{q}_T^{*f} S^{0y}_{f,l} - \mathbf{q}_T^{*f} S^{0y}_{f,r} \right\} . \mathbf{j} \\ + \left\{ \mathbf{q}_T^{*f} S_f \right\}_{k+\frac{1}{2}} - \left\{ \mathbf{q}_T^{*f} S_f \right\}_{k-\frac{1}{2}} + \left\{ \mathbf{q}_T^{*s} S_s \right\}_{k+\frac{1}{2}} - \left\{ \mathbf{q}_T^{*s} S_s \right\}_{k-\frac{1}{2}} + \sum \left\{ \mathbf{q}_T^{*f} S^{0z}_{f,l} - \mathbf{q}_T^{*f} S^{0z}_{f,r} \right\} . \mathbf{k} \\ + h_c \sum_{l=1}^{N} \left(S_{obst}\right)_l \left(T_{i,j,k} - (T_{wall})_l\right) \end{array} \right).$$

We now address two phase flow modeling

5 Particles plume modeling

In this section, a new sub-model for dispersed suspensions dynamics is derived. The conventional Eulerian formulation used in most two-phase dilute suspensions codes is based on the pressureless gas dynamics equations coupled to the gas dynamics equations through source terms. The pressureless equations present at least two weaknesses. First, the system is hyperbolic degenerate. Second, the model is unable to model particles jets dispersion and in particular plume dynamics. Indeed, the particle phase system is coupled to the gas phase system through drag, heat and mass transfer effects. No turbulent effect nor dispersion effect are considered. To overcome these drawbacks turbulent effects have been introduced in [44] yielding in a strictly hyperbolic system able to model plumes with the help of a single turbulent viscosity parameter. However, difficulties appeared for numerical resolution, especially in severe conditions such as explosions. Indeed, the turbulent sound speed present in the model is very low, resulting in particles vacuum appearance yielding code failure. Also, the various boundary conditions need very accurate treatment, even in zones where particles are absent (i.e. very low concentration). To improve model robustness a semi-discrete asymptotic analysis is achieved following the lines of [41]. The hyperbolic model of [44] is used as starting point and a new reduced model is built, corresponding to a viscous regularization of the pressureless gas dynamics equations. The new model is easy to solve and particularly robust. It is able to reproduce literature experimental data of plumes with a single viscosity parameter.
The hyperbolic turbulent model of dispersed flows is first recall from [44] and then reduced with the semi discrete method.

5.1 Hyperbolic turbulent model for particles flows

The model developed in [44] corresponds to the Euler equations where the thermodynamic pressure is replaced by a turbulent pressure. There is also a turbulent viscosity appearing in the momentum, and in the energy equations. This turbulent formulation improves the mathematical features of the system as well as the particles flow behavior. In particular, it allows particles jets enlargement. This model has been validated with the help of experimental data of [50] and [51]. The turbulent model reads:

$$\begin{cases} \dfrac{\partial \rho_p}{\partial t} + \nabla.(\rho_p \mathbf{u}_p) & = 0 \\ \dfrac{\partial \rho \mathbf{u}_p}{\partial t} + \nabla.(\rho_p \mathbf{u}_p \otimes \mathbf{u}_p + P_{pt}\mathbb{I}) & = \mathbf{F}_{g\to p} + \nabla.\left(\mu_t \nabla \mathbf{u}_p\right) \\ \dfrac{\partial \rho_p E_p}{\partial t} + \nabla.(\rho_p E_p \mathbf{u}_p + P_{pt}\mathbf{u}_p) & = \mathbf{u}_p \mathbf{F}_{g\to p} + \nabla.\left(\mu_t \mathbf{u}_p^T \nabla \mathbf{u}_p\right) \\ \dfrac{\partial \rho_p e_p}{\partial t} + \nabla.(\rho_p \mathbf{u}_p e_p) & = 0 \end{cases} \tag{9}$$

Where, $\rho_p = \alpha_p \rho_c$ represents the particles apparent density, defined as the product of the particles volume fraction α_p and the condensed phase density ρ_c. The particle velocity vector is denoted by $\mathbf{u_p}$ while P_{pt} represents the particles turbulent pressure. It is determined with the help of the turbulent equation of state [45]:

$$P_{pt} = (\gamma_t - 1)\rho_p e_{pt}.$$

The turbulent polytropic coefficient is equal to 3, 2 and 5/3 respectively for 1D, 2D and 3D flows. The turbulent particles energy is obtained from the total energy definition and associated evolution equations (Total energy and internal energy equations).

$$E_p = \frac{\|\mathbf{u_p}\|}{2} + e_p(T) + e_{pt}(\rho_p, P_{pt}).$$

The fluxes involves a turbulent pressure, making the equations system strictly hyperbolic with the waves speeds $u_p,\ u_p + c_{pt},$ and $u_p + c_{pt}$. Turbulent square sound speed is given by,

$$c_{pt}^2 = \frac{\gamma_t P_{pt}}{\rho_{pt}}.$$

On the right hand side, drag terms appear (details are given in Appendix B). There is also turbulent tensor involving a single parameter μ_t. This formulation is compatible with the second law of thermodynamics, as the turbulent entropy equations reads,

$$\frac{\partial \rho_p s_{pt}}{\partial t} + \nabla.(\rho_p \mathbf{u}_p s_{pt}) = \mu_t Tr\left\{(\nabla \mathbf{u}_p).(\nabla \mathbf{u}_p)^T\right\} \geq 0. \tag{10}$$

where s_{pt} represents the particles turbulent entropy, given by:

$$s_{pt} = \frac{P_{pt}}{(\rho_p)^{\gamma_t}}.$$

Obviously, it implies positive entropy production for the system. The aim is to reduce the model maintaining the same accuracy as reported in [44] while improving its robustness.

5.2 Turbulent model reduction

The hyperbolic part of system (9) can be written as follows (one dimensional case),

$$\frac{\partial \mathbf{U}}{\partial t} + \frac{\partial \mathbf{F}}{\partial x} = 0$$

with,

$$\mathbf{U} = (\rho_p, \rho_p u_p, \rho_p E_p, \rho_p e_p)^T$$

$$\mathbf{F} = \left(\rho_p u_p, \rho_p u_p^2 + P_{pt}, \rho_p E_p u_p + P_{pt} u_p, \rho_p e_p u_p\right)^T.$$

Let us consider the Godunov scheme,

$$U_i^{n+1} = U_i^n - \frac{\Delta t}{\Delta x}\left(F^*_{i+1/2} - F^*_{i-1/2}\right) \tag{11}$$

with the Rusanov flux [42] at each cell boundaries.

$$F^* = \frac{F_R + F_L}{2} + \frac{S}{2}\left(U_L - U_R\right) \tag{12}$$

The Rusanov numerical flux is considered for simplicity reasons. More sophisticated approximate Riemann solver can be considered as well. With the Rusanov solver, the wave speed S is usually taken as the maximum wave speed at a given cell boundary. The Godunov scheme (11) thus becomes:

$$\begin{aligned} \frac{U_i^{n+1} - U_i^n}{\Delta t} &+ \frac{1}{2\Delta x}\left((F_{i+1} + F_i) - (F_i + F_{i-1})\right) \\ &+ \frac{1}{2\Delta x}\left(S_{i+1/2}(U_i - U_{i+1}) - S_{i-1/2}(U_{i-1} - U_i)\right) = 0 \end{aligned}$$

Rearranging this expression, under the assumption that $S_{i+1/2} = S_{i-1/2} = S$ yields,

$$\frac{U_i^{n+1} - U_i^n}{\Delta t} + \frac{F_{i+1}^n - F_{i-1}^n}{2\Delta x} = \frac{S\Delta x}{2}\,\frac{U_{1+1}^n - 2U_i^n + U_{i-1}^n}{\Delta x^2} \tag{13}$$

This method is used to evolve the hyperbolic system (9), that can be expressed with the following set of variables: $\mathbf{U} = (\rho_p, \rho_p u_p, \rho_p E_p, \rho_p e_p)^T$, or alternatively, $\mathbf{U} = (\rho_p, \rho_p u_p, \rho_p E_p, \rho_p s_p)^T$
Lets consider the second option. After each hyperbolic step (13), the following dissipation step is considered:

$$\begin{cases} \dfrac{\partial \rho \mathbf{u}_p}{\partial t} & = \nabla.\left(\mu_t \nabla \mathbf{u}_p\right) \\ \dfrac{\partial \rho_p E_p}{\partial t} & = \nabla.\left(\mu_t \mathbf{u}_p^T \nabla \mathbf{u}_p\right) \\ \dfrac{\partial \rho_p s_{pt}}{\partial t} & = \mu_t Tr\left((\nabla \mathbf{u}_p).(\nabla \mathbf{u}_p)^T\right) \end{cases}$$

Initially, the particles turbulent entropy is zero everywhere, at least for particles plumes. Then, the production occurs through the term $\mu_t Tr\left((\nabla \mathbf{u}_p).(\nabla \mathbf{u}_p)^T\right)$ and the turbulent entropy increases, creating the turbulent pressure that produces particles jets enlargement. However, the turbulent viscosity is weak ($\mu_t = 2.10^{-3} kg.m^{-1}.s^{-1}$) resulting in low turbulent entropy and pressure creation. Typical computed turbulent pressures are of the order of a few Pascals. In the asymptotic limit of vanishing turbulent viscosity, the entropy equation reduces to:

$$\frac{\partial \rho_p s_{pt}}{\partial t} = 0.$$

Consequently, the turbulent pressure vanishes too. In this limit of vanishing turbulent viscosity, the continuous limit of the discrete equation (13) reads:

$$\begin{cases} \dfrac{\partial \rho_p}{\partial t} + \nabla.\left(\rho_p \mathbf{u}_p\right) = D_p \Delta \rho_p \\ \dfrac{\partial \rho_p \mathbf{u}_p}{\partial t} + \nabla.\left(\rho_p \mathbf{u}_p \otimes \mathbf{u}_p\right) = D_p \Delta(\rho_p \mathbf{u_p}) + \mathbf{F}_{g\to p} \\ \dfrac{\partial \rho_p E_p}{\partial t} + \nabla.\left(\rho_p E_p \mathbf{u}_p\right) = D_p \Delta(\rho_p E_p) + \mathbf{F}_{g\to p}.\mathbf{u}_p \end{cases} \tag{14}$$

Diffusion terms appear with conservative variables as arguments and the same diffusion coefficient for all equations. Obviously, these equations can be written in divergence form:

$$\begin{cases} \dfrac{\partial \rho_p}{\partial t} + \nabla.\left(\rho_p \mathbf{u}_p - D_p \nabla.\rho_p\right) = 0 \\ \dfrac{\partial \rho_p \mathbf{u}_p}{\partial t} + \nabla.\left(\rho_p \mathbf{u}_p \otimes \mathbf{u}_p - D_p \nabla.(\rho_p \mathbf{u_p})\right) = \mathbf{F}_{g\to p} \\ \dfrac{\partial \rho_p E_p}{\partial t} + \nabla.\left(\rho_p E_p \mathbf{u}_p - D_p \nabla(\rho_p E_p)\right) = \mathbf{F}_{g\to p}.\mathbf{u}_p \end{cases} \tag{15}$$

This system corresponds to the pressureless Euler equations with turbulent diffusion. Obviously, it is reminiscent of artificial viscosity formulations. The key point is related to the second law of thermodynamics associated to this model. As mentioned in [41] with the Euler equations of gas dynamics

as example, augmented by the same artificial viscosity terms, there is no hope that the second law of thermodynamics be fulfilled in the local sense. However, similarly as artificial viscosity numerical methods, discontinuities are captured and the second law of thermodynamics is fulfilled in the weak sense, which corresponds to the correct formulation of the second principle of thermodynamics. Here, as System (9) is in local agreement with the second law of thermodynamics, System (15) is necessarily in agreement too with the second law, in the global sense.
A resolution method for the pressureless model is detailed in [46], where the model is studied without artificial diffusion. In the right hand side of the equations, the viscous drag force $\mathbf{F_{g\to p}}$ appears as well as the turbulent diffusion terms for which the diffusion coefficient D_p must be determined. Its determination is addressed with the help of experiments.

5.3 Turbulent coefficient determination

The aim is to determine the diffusion coefficient D_p. In [44], a unique value of turbulent viscosity was determined ($\mu_t = 2.10^{-3}\ kg.m^{-1}.s^{-1}$) to reproduce the experimental dispersed particle jets of [50] and [51] with very good agreement. The same experiments are used to determine the turbulent diffusion coefficient of the present reduced model.

5.3.1 Comparisons with experimental data

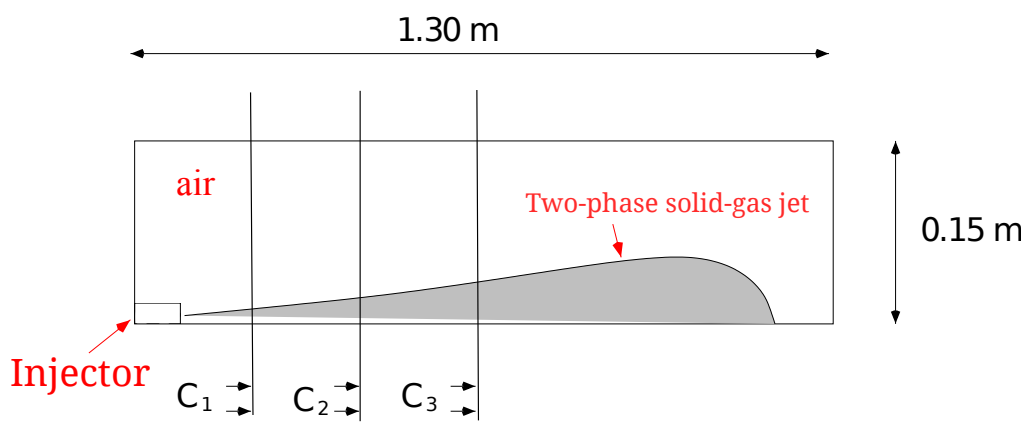

Figure 11: Schematic representation of the two-phase jet experimental configuration.

Two different set of experimental data are used to study particles jets dispersion. Details on the experimental facilities and configurations are given in [50] and [51]. These experiments are interesting as very different materials are used, with different densities and particle sizes. A schematic representation of the studied configuration is shown in Figure 11.

	Tsuji [51]	Hishida [50]
Particles diameters (μm)	500	64
Material density (kg/m^3)	1020	2590
Injection velocity (m/s)	24	30
Apparent density at injector(kg/m^3)	0.2	1.0
Injector diameter **D** (mm)	20	13

Table 1: Experimental configuration data from [50] and [51].

As shown in Figures 12 and 13, good agreement is obtained for both sets of experimental data. It is worth to mention that the product of the diffusion coefficient by the apparent density at injection is the same for both experiments and is also very close to the turbulent viscosity used in [44].

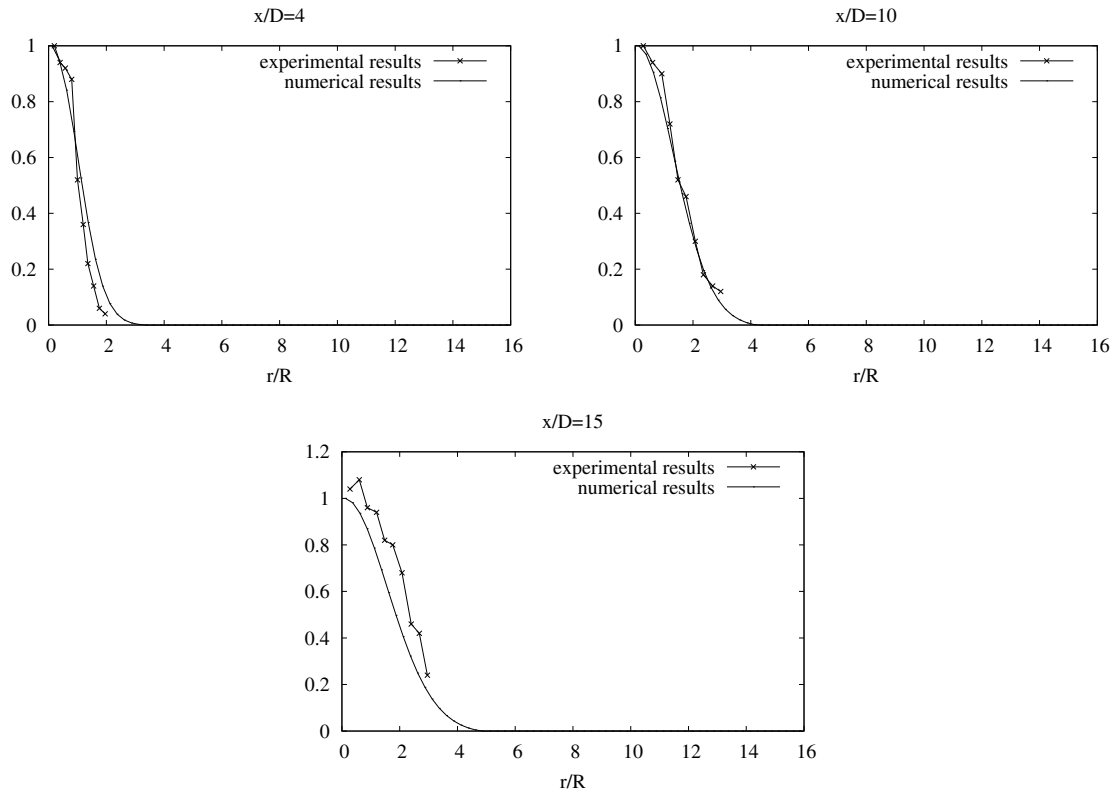

Figure 12: Computed results in lines versus experimental data of [51]. Normalized apparent density ρ_p/ρ_{p0} cross cut at abscissa $C_1 = 4D$, $C_2 = 10D$ and $C_3 = 15D$ (with ρ_{p0} the apparent density along the centerline). The jet width increases during its progression. The diffusion coefficient in the numerical model is such that $D_p\rho_p = 1.5\ 10^{-3} kg.m^{-1}.s^{-1}$.

To appreciate the effects of turbulent diffusion in the pressureless equations, we compare the results obtained using the turbulent model of [44] with those

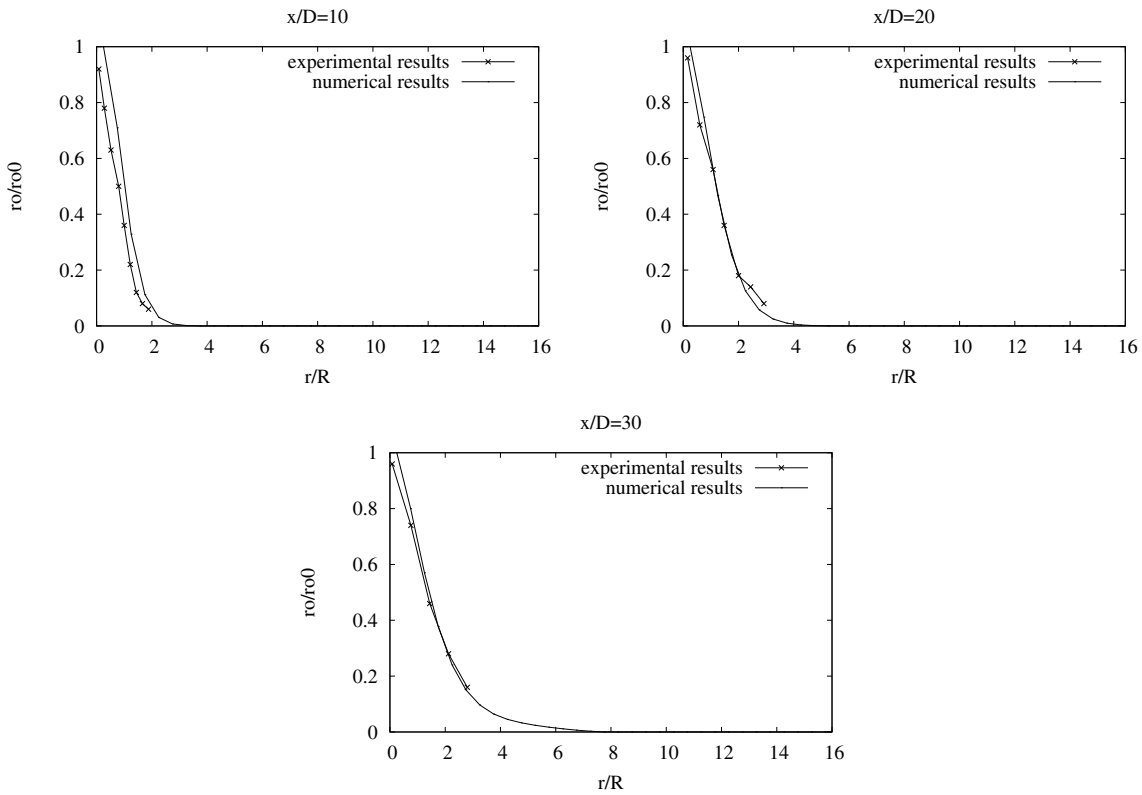

Figure 13: Computed results in lines versus experimental data of [50]. Normalized apparent density ρ_p/ρ_{p0} cross cut at abscissa $C_1 = 10D$, $C_2 = 20D$ and $C_3 = 30D$ (with ρ_{p0} the apparent density along the centerline). The jet width increases during its progression. The diffusion coefficient in the numerical model is again $D_p\rho_p = 1.5\ 10^{-3} kg.m^{-1}.s^{-1}$.

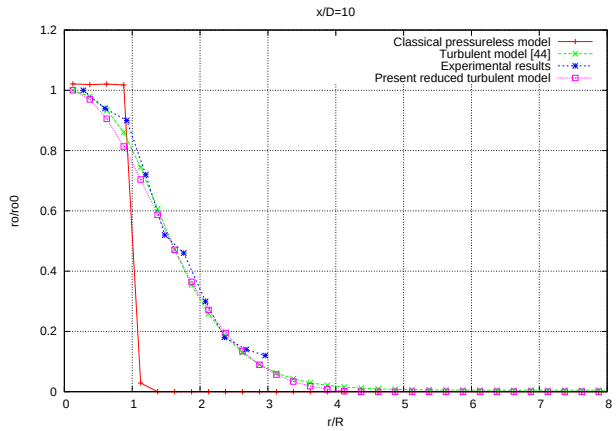

Figure 14: Comparison of the results obtained with the different models on the configuration of [51].

obtained with the conventional pressureless model and the results with the reduced model in the configuration of [51]. The comparison is shown in Figure 14. The reduced model and the parent turbulent one gives similar results. Both models allow jet enlargement with good agreement with the experimental results while the jets computed with the pressureless model shows no enlargement.

6 Topography

The discrete formulation of heterogeneous media described in section 2 and its various extensions described in the preceding sections are extended to the consideration of realistic topographies such as those of urban and country places.

6.1 Urban places

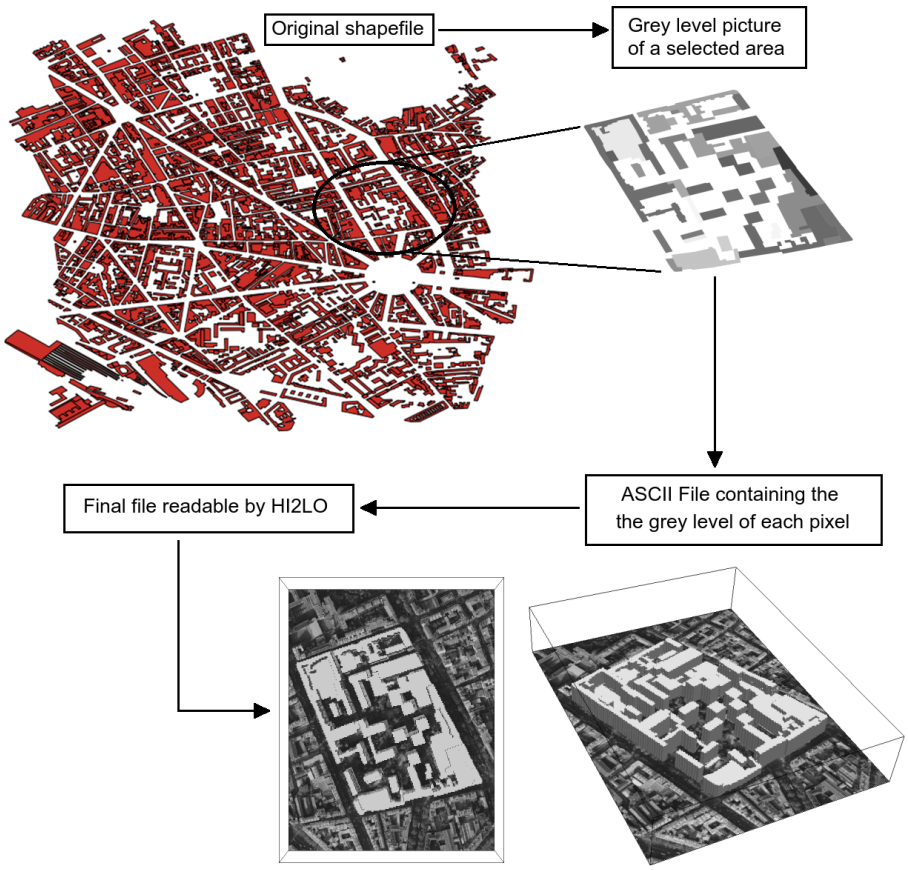

Figure 15: Representation of the various files and format treatment to get a readable file for a CFD code, starting from a shapefile.

It is necessary to have a 'shapefile' containing data associated to the considered topography, these files can be bought or built. Real topography is generated using a Geographic Information System (GIS). Several softwares are able to edit and manage shapefiles, such as for example Quantum GIS. In this frame, buildings are represented as polygones. The first step in the present context is related to the geometry building for the CFD code with a preprocessing tool, based on the treatment of gray levels. The procedure is schematized in the Figure 15.

The aim is to rebuilt the urban geometry using the gray levels, each one corresponding to an elevation. To do this, the gray picture is exported to an ASCII file containing the gray level of each pixel with the help of the ImageJ free software [32]. The resulting file is then treated by another firmware code which writes a new ASCII file considering the CFD code mesh (cartesian) and transforming the gray levels in real elevations. The final file is thus obtained and is readable by the HI2LO code.

6.2 Countries and large scales

When dealing with large scales, topography is built with the help of numerical elevation data available on the web (USGS, IGN). These files are usually not adapted to Cartesian grids computations. In this case too, a preprocessing tool has been developed to create files readable by the final code. The aim is to obtain a readable file for different type of elevation data.

The procedure is summarized in Figure 16. The preprocessing tool al-

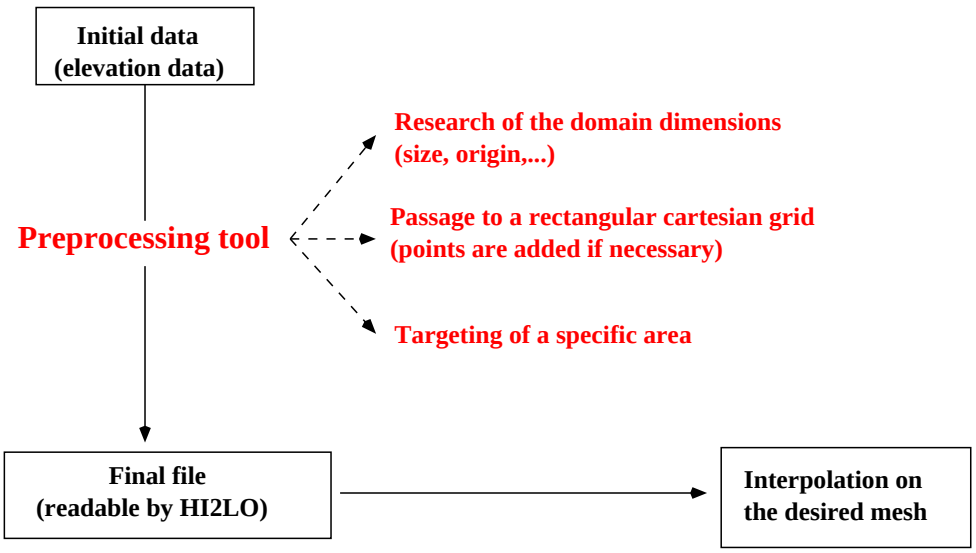

Figure 16: Procedure to build the ASCII file readable by HI2LO.

lows to add geographical boundaries at the reconstructed map and thus to focus on a specific area of it. Thus a complete map, or a part of it, can be reconstructed . Figure 17 shows the Martinique island map which has been rebuilt. The preprocessing tool is thus able to build a large range of

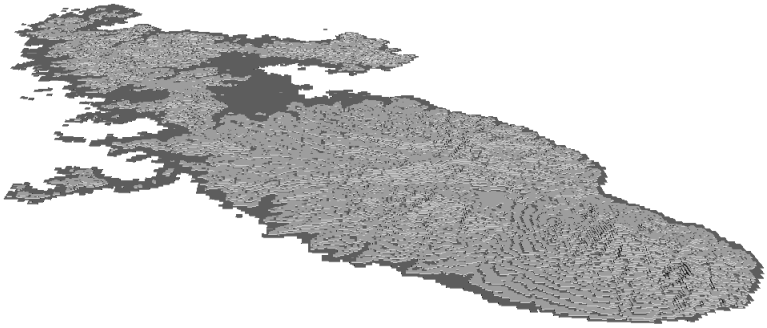

Figure 17: Representation of the Martinique island from an elevation file.

topographies using different kind of elevation data: xyz files, digital elevation models, or shapefiles. In the following section, computational examples in 3D are shown.

7 Examples

In this section, various configurations are considered as computational examples.

7.1 Explosion in urban place

The first example corresponds to a simulation of a 100 kg TNT charge explosion in a street in the city of Marseille (France). The explosion is modeled as a constant volume explosion, corresponding to the initial pressure of 85711 Bar and density of $1604 kg/m^3$. Detonation products are considered as ideal gases with $\gamma = 3$, even if this assumption is inacurate at high density levels, that corresponds to very short time events. Topography of the neighborhood has been modeled with a shapefile. Solid particles are present around the charge in this computation, the features of these particles being the following,

$$D = 30\mu m, \quad \rho_p = 3kg/m^3, \rho^* = 1200kg/m^3,$$

with D, the particles diameter, ρ_p the apparent density and ρ^*, the real density of the material.

Figure 18, shows the detonation product mass fraction at different times and Figure 19 shows the particles apparent density at several instants. Figure

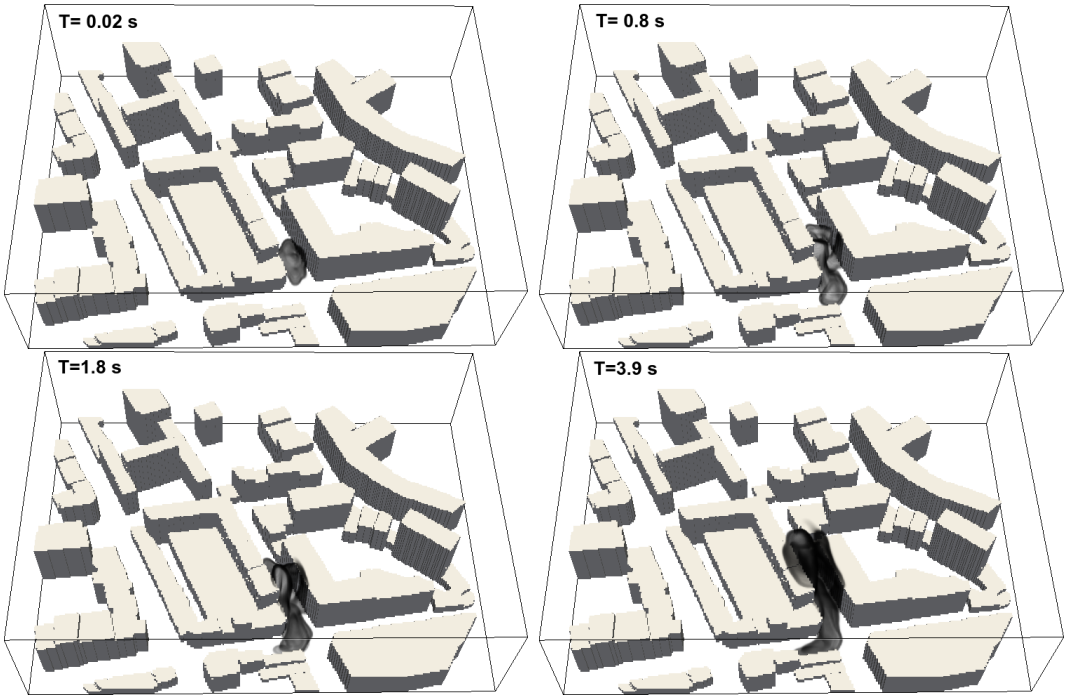

Figure 18: Contours of the detonation products mass fraction at times : 0.02s, 0.8s, 1.8s and 3.9s

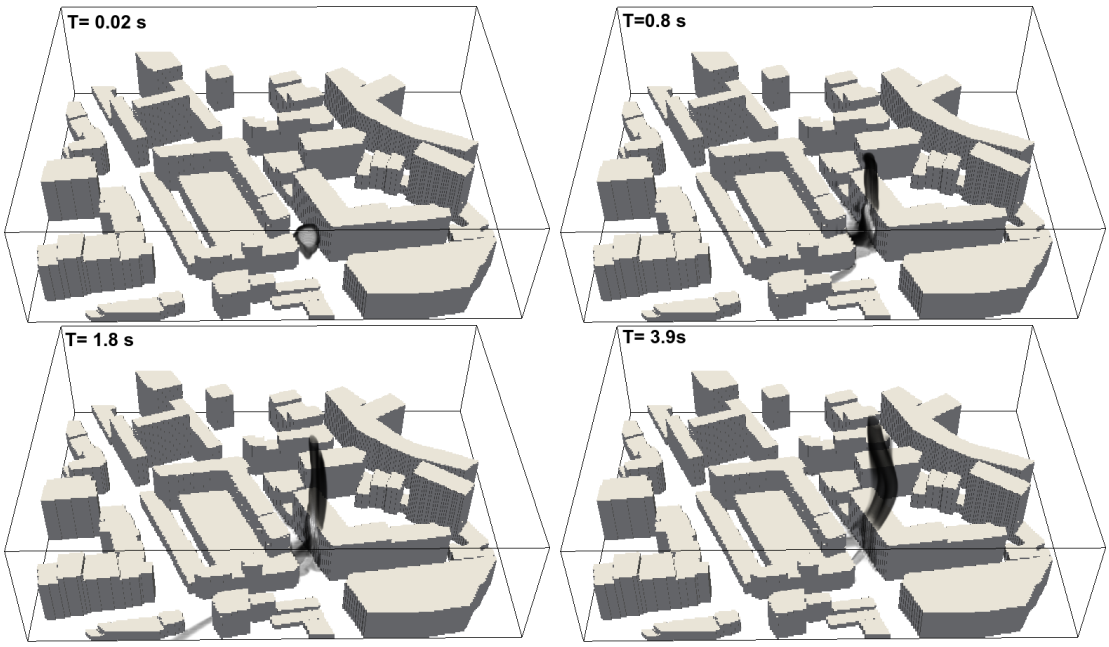

Figure 19: Contours of the particle apparent density at different times: 0.02s, 0.8s, 1.8s and 3.9s

20 shows the pressure contour at six instants giving the shock wave location

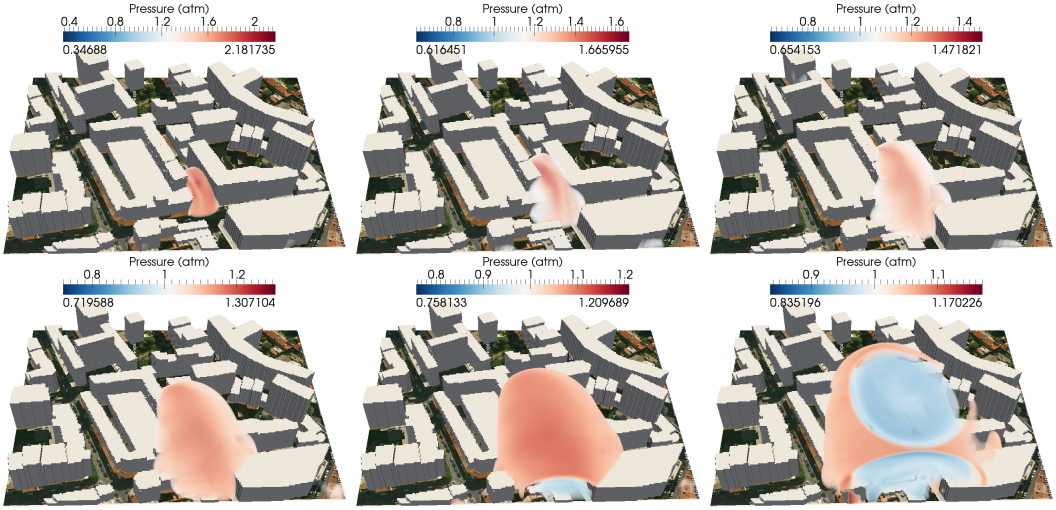

Figure 20: Contours of the pressure at several instants: 20 ms, 40 ms, 60 ms, 80 ms, 100 s and 140 ms.

in the three dimensional domain.
In Figure 21, cut view of pressure contours at 1 m high are shown. We can see the propagation of the shock wave and its interaction with the buildings.

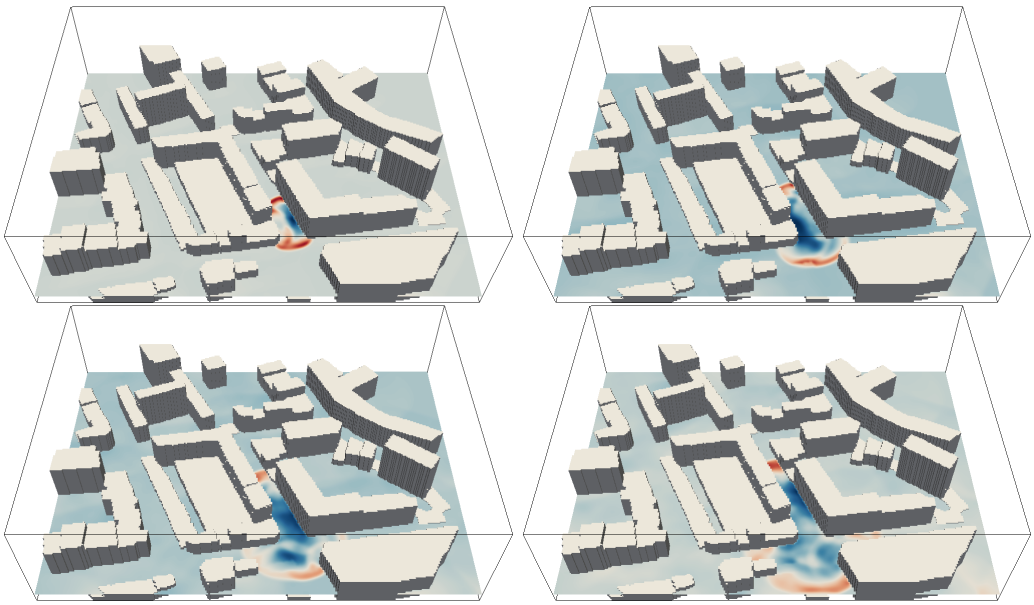

Figure 21: Volume representation of the pressure at four instants: 20 ms, 40 ms, 60 ms and 80 ms.

These computations are done without heat and mass exchanges with the buildings.

7.2 Gas dispersion on large domains

In this second example, the formation and dispersion of a gas chemical species cloud is studied. The topography of the domain under consideration is rebuilt with the help of digital elevation data. A part of the Umnak island (Alaska, USA) as shown in Figure 22 is considered.

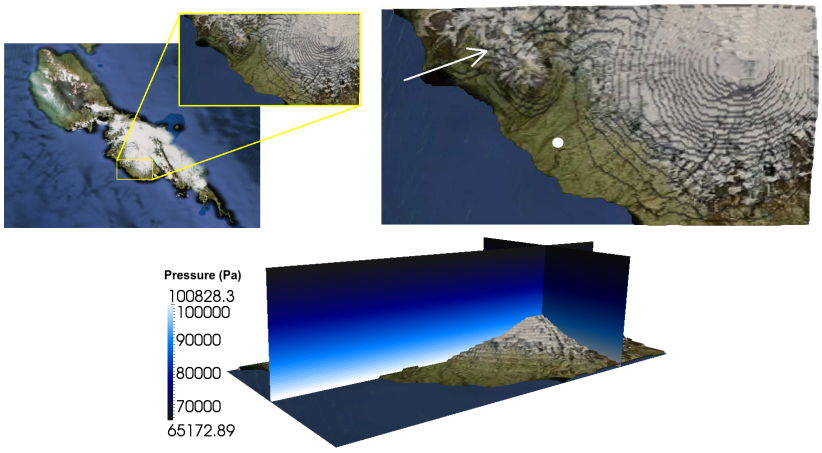

Figure 22: Upper left: Domain under consideration (16 km long, 8 km wide and 4 km high). Upper right: direction of the wind and position of the tank (White circle). On bottom: Initial conditions for the pressure.

The aim relies in the computation of the formation and propagation of a gas cloud issued of a ruptured vessel. An internal obstacle embedded in the mesh is considered with an outflow connected to a tank during a limited time with the following boundary conditions:

$$P_0 = 150\ Bar, \qquad T_0 = 600K,$$
$$Y_{air} = 0.98, \qquad Y_{CO_2} = 0.02.$$

After that time, the tank boundary condition becomes a simple wall. Atmospheric boundary conditions for the wind are supposed to vary according to the following profile [34],[35],[33]:

$$\mathbf{u}(z) = \mathbf{u}(z_0)\left(\frac{z}{z_0}\right)^{0.29},$$

where $\mathbf{u}(z_0) = (6\ m/s, 2\ m/s, 0)^t$ corresponds to the velocity vector at the altitude $z_0 = 100\ m$. Conditions of stratified atmosphere are used as initial conditions, the various flow variables depending on the height z. To do this, an adiabatic transformation is considered between the ground and the top of the domain. The final physical time is 13 min 20s. Figures 23 and 24 show the gas plume at different instants. These pictures show the plume dispersion which is subjected to the topography of the domain and to the wind profile.

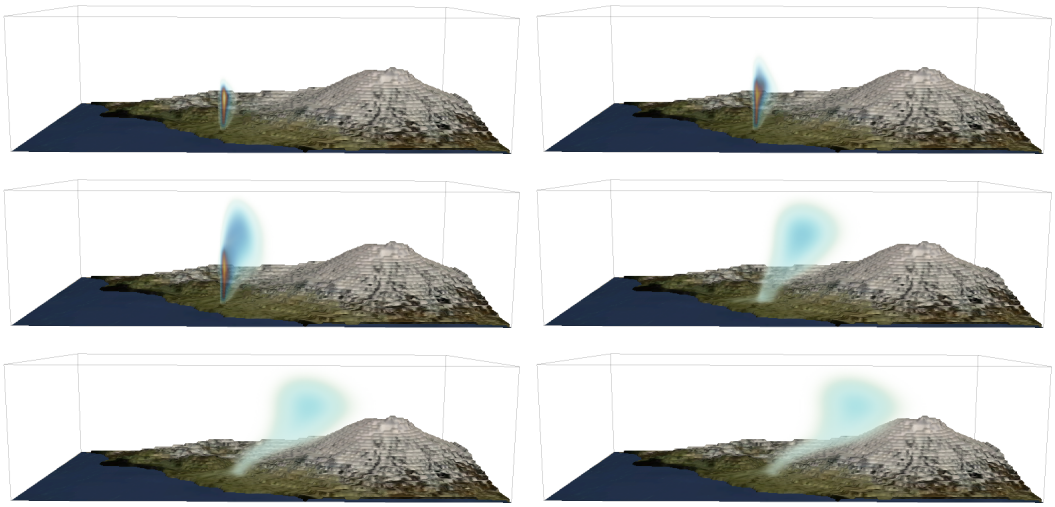

Figure 23: Contours of CO_2 mass fraction at different times: t=40 s, t=100s, t=220s, t=420s, t=620s and t=800 s. Gas injection is interrupted after 200 s.

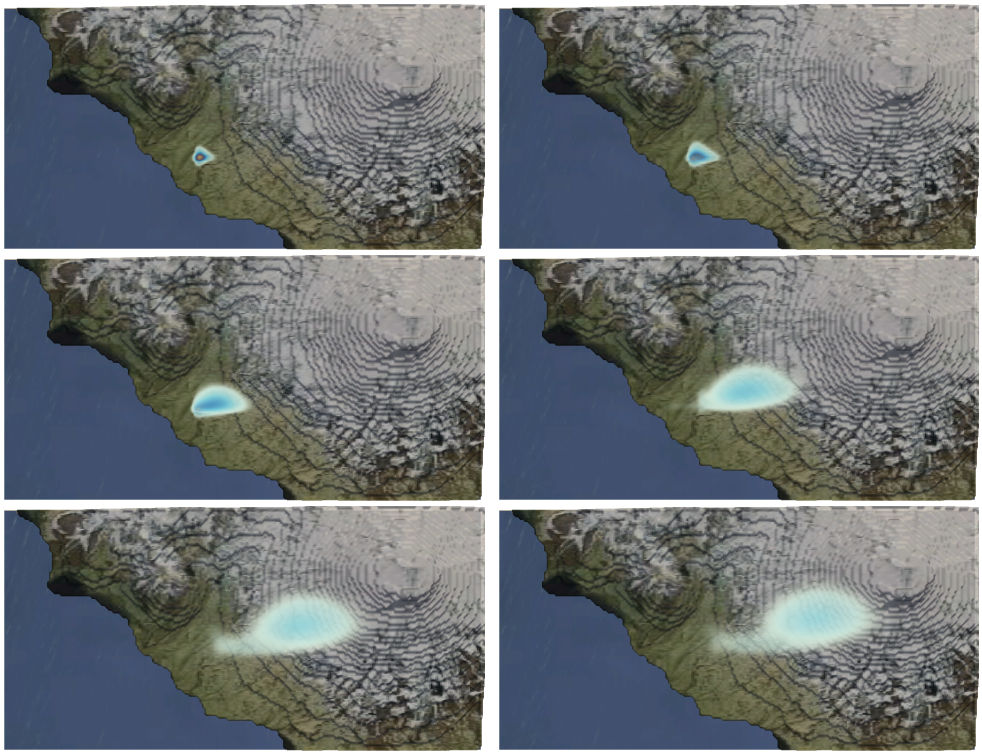

Figure 24: Contours of CO_2 mass fraction at different times, top view at times: t=40 s, t=100s, t=220s, t=420s, t=620s and t=800 s.

8 Conclusion and future works

In this paper a new computational fluid dynamics code for safety analysis is presented. It is able to consider highly heterogeneous media such as

cities, hilly grounds or other geometrical domains. Its structure and formulation enable the consideration of complex domains quite easily. The physics considered at present corresponds to gas mixtures, with transport, wave propagation, heat and mass diffusion, at both molecular and turbulent scales, as well as particles cloud dynamics. The simulation code is parrallel. It is planned to extend its capabilities to low Mach number flow conditions [36,37,38]. It is also planned to couple this code with other multiphase flow codes considering advanced detonation modeling [40,39] to achieve accurate explosion computations, in particular in highly dynamics conditions, for time scales less than $1ms$.

References

[1] Rose, T.A. (2003), *Air3D user guide. 7.0: RMCS*, UK: Cranfield University

[2] Cowler, M.S and Birnbaum, N.K. (1989), *AUTODYN user manual.* Century Dynamics Inc, Oakland, CA (USA)

[3] Crepeau, J. Needham, C. and Hikida, S. (2001), *SHAMRC Second-Order Hydrodynamic Automatic Mesh Refinement Code Vol 1: Methodology*, Applied Research Associates, Albuquerque, NM.

[4] Boybeyi, Z. Löhner, R. and Ananthakrishna, S. (2007), *A Godunov-type scheme for atmospheric flows on unstructured grids: Euler and Navier-Stokes equations*, Pure and Applied Geophysics 164(1), 217-244.

[5] Lohner, R. Yang, C. Cebral, J. Soto, O., Camelli, O., Baum, J.D., Luo, H., Mestreau, E.and Sharov, D. (2001), *Advances in FEFLO*, AIAA Aerospace Sciences Meeting & Exhibit, 40 th, Reno, NV.

[6] Hanna S.R., Tehranian S., Carissimo B., Mac Donald R.W., and Lohner R. (2002), *Comparisons of model simulations with observations of mean flow and turbulence within simple obstacle arrays*, Atmospheric Environment 36(32), 5067-5079

[7] Camelli, F.E. Hanna S.R., Lohner R. O., Baum J.D., Luo H., Mestreau E., and Sharov D., (2006), *FEFLO CFD model study of flow and dispersion as influenced by tall buildings in New York city*, In 86th Annual Meeting of the American Meteorological Society, Sixth Symposium on Urban Environment, Atlanta, USA.

[8] Hanna S.R., Hansen O.R., and Dharmavaram S. (2004), *FLACS CFD air quality model performance evaluation with Kit Fox, MUST, Prairie Grass, and EMU observations*, Atmospheric Environment, 38(28), 4675-4687.

[9] Hanna S.R., Hansen O.R., Ichard M. and Strimaitis D., (2009), *CFD model simulation of dispersion from chlorine railcar releases in industrial and urban areas*, Atmospheric Environment, 43(2), 262-270.

[10] Britter R.E. and Hanna S.R. (2009), *Flow and dispersion in urban areas*, Annual Review of Fluid Mechanics, 35(1), 469-496.

[11] Middha P., Hansen O.R. and Storvik I.E., (2009), *Validation of CFD-model for hydrogen dispersion*, Journal of Loss Prevention in the Process Industries, 22(6), 1034-1038.

[12] Hansen OR., Gavelli F., Ichard M. and Davis SG. (2010), *Validation of FLACS against experimental data sets from the model evaluation database for LNG vapor dispersion*, Journal of Loss Prevention in the Process Industries, 23(6) 857-877.

[13] Coirier W.J., Fricker D.M., Furmanczyk M. and Kim S., (2005), *A computational fluid dynamics approach for urban area transport and dispersion modeling*, Environmental Fluid Mechanics, 5(5), 443-479.

[14] Le Métayer O., Massol A., Favrie N., and Hank S., (2011), *A discrete model for compressible flows in heterogeneous media.* Journal of Computational Physics, 230(7), 2470-2495.

[15] Abgrall R. and Saurel R., (2003), *Discrete equations for physical and numerical compressible multiphase mixtures.* Journal of Computational Physics, 186(2) 361-396

[16] Le Métayer O., Massoni J. and Saurel R., (2005), *Modelling evaporation fronts with reactive Riemann solvers.* Journal of Computational Physics, 205(2), 567-610

[17] Colella P., Graves D.T., Keen B.J. and Modiano D., (2006), *A Cartesian grid embedded boundary method for hyperbolic conservation laws.* Journal of Computational Physics, 211(1), 347-366.

[18] Johansen H. and Colella P.,(1998), *A Cartesian grid embedded boundary method for Poisson's equation on irregular domains.* Journal of Computational Physics, 147(1), 60-85.

[19] Toro E.F. (1997), *Riemann solvers and numerical methods for fluid dynamics: a practical introduction.* Springer-Verlag

[20] Toro E.F., Spruce M. and Speares W., (1994), *Restoration of the contact surface in the HLL-Riemann solver.* Shock waves, V 4 N0 1 p 25–34

[21] Jourdan G., Biamino L., Mariani C., Houas L., Massol A., Igra O., (2009), *Experimental study of the mitigation of a shock wave through a system of plates.* Proceedings of the 27th International Symposium on Shock Waves, Saint-Petersburg, Russia, July 2009.

[22] Trelat S., (2006), *Impact de fortes explosions sur les bâtiments représentatifs dune installation industrielle.* Phd Thesis University of Orlans (France)

[23] Trelat S., Sochet I., Autrusson B., Loiseau O. and Cheval K.,(2007), *Strong explosion near a parallelepipedic structure*. Shock Waves, 16(4), 349-357.

[24] Toro E.F., Millington R.C and Nejad L.A.M., (2001), *Towards very high order Godunov schemes*. Godunov Methods. Theory and Applications, Kluwer/Plenum Academic Publishers, 905-938

[25] Titarev V.A and Toro E.F., (2002), *ADER: Arbitrary high order Godunov approach*. Journal of Scientific Computing, 17(1), 609-618.

[26] Harten A., Engquist B., Osher S., Chakravarthy S.R., (1987), *Uniformly high order accurate essentially non-oscillatory schemes, III*. Journal of Computational Physics, 71(2) 231-303.

[27] Liu X.D., Osher S. and Chan T., (1994), *Weighted essentially non-oscillatory schemes*. Journal of Computational Physics, 115(1), 200-212

[28] Jiang G.S. and Shu C.W. (1996), *Efficient Implementation of Weighted ENO Schemes*. Journal of Computational Physics, 126(1) 202-228

[29] Giovangigli, V. (1999), *Multicomponent flow modeling*, ISBN 0817640487, Birkhauser

[30] Hanna S.R., Briggs G.A. and Hosker Jr. R.P.,(1982), *Handbook on atmospheric diffusion*. Atmospheric Turbulence and Diffusion Lab., National Oceanic and Atmospheric Administration, Oak Ridge, TN (USA).

[31] Rose T.A. and Smith P.D. (2002), *Influence of the principal geometrical parameters of straight city streets on positive and negative phase blast wave impulses*. International Journal of Impact Engineering ,27(4), 359-376.

[32] Abramoff M.D., Magalhaes P.J. and Ram S.J.,(2004) *Image processing with ImageJ*, Biophotonics international, 11(7), p 36-42, Laurin Publishing (rsbweb.nih.gov/ij/)

[33] Touma J.S, (1977). *Dependence of the wind profile power law on stability for various locations.*. Air Pollution Control Association, Journal, NC, 27(9), 863-866

[34] DeMarrais G.A., (1959). *Wind-Speed Profiles at Brookhaven National Laboratory*. Journal of Atmospheric Sciences, 16, 181-190

[35] Davenport A.G., (1963). *The relationship of wind structure to wind loading*. proceedings of the conference on wind effect on structures, 1, 54-102.

[36] Turkel E., (1987). *Preconditioned methods for solving the incompressible and low speed compressible equations*. Journal of computational physics, 72(2),277-298.

[37] Guillard H. and Viozat C., (1999). *On the behaviour of upwind schemes in the low Mach number limit*. Computers and fluids, 28(1), 63-86.

[38] Le Martelot S., Nkonga B. and Saurel R. (2013). *Liquid and liquid-gas flows at all speeds*, Journal of Computational Physics, 255(15), 53-82.

[39] Schoch S., Nikiforakis N., Lee B.J and Saurel R., (2013). *Multi-phase simulation of ammonium nitrate emulsion detonations*, Combustion and Flame 160(9), 1883-1899.

[40] Petitpas F., Saurel R., Franquet E. and Chinnayya A, (2009). *Modelling detonation waves in condensed energetic materials: Multiphase CJ conditions and multidimensional computations*, Shock waves 19(5), 377-401

[41] Saurel R., Huber G., Jourdan G., Lapébie E. and Munier L., (2012), *Modelling spherical explosions with turbulent mixing and post-detonation*, Physics of Fluids 24(5), 5101-2012

[42] Rusanov V.V., (1961). *The calculation of the interaction of non-stationary shock waves and obstacles*, USSR Journal of Computational Mathematics and Physics, USSR, 1 267-279.

[43] Rudinger G., (1965). *Some effects of finite particle volume on the dynamics of gas-particle mixtures*, AIAA journal, 3(7), 1217-1222 .

[44] Hank S., Saurel R., and Le Metayer O., (2011), *A Hyperbolic Eulerian Model for Dilute Two-Phase Suspensions*, Journal of Modern Physics, 2, 997-1011.

[45] Saurel R., Chinnayya A. and Renaud F., (2003), *Thermodynamic analysis and numerical resolution of a turbulent-fully ionized plasma flow model.* Shock Waves, 13(4), 283-297.

[46] Saurel R., Daniel E. and Loraud J.C., (1994), *Two-phase flows-Second-order schemes and boundary conditions.* AIAA journal, 32(6), 1214-1221.

[47] Schiller L., and Naumann Z., (1935), *A drag coefficient correlation.* V.D.I. Zeitung 77,318-320

[48] Knudsen J.G. and Katz D.L., (1958), *Fluid mechanics and heat transfer.* McGraw-Mill, New York, p 511

[49] Clift R., Grace J.R. and Weber ME., (1978), *Bubbles, Drops and Particles.* Academic, New York.

[50] Hishida K., Kaneko K., and Maeda M., (1985), *Turbulence structure of a gas-solid two phase circular jet*, Trans. JSME 51, 2330-2337 *In Japanese.*.

[51] Tsuji Y., Morikawa Y., Tanaka T., Karimine K. and Nishida S., (1988), *Measurement of an axisymmetric jet laden with coarse particles*, International Journal of Multiphase Flow, 14, 565–574.

[52] Wilke C.R., (1950), *A viscosity equation for gas mixtures*, The Journal of Chemical Physics, 18, 517.

[53] Lindsay A. L. and Bromley L. A., (1950), *Thermal conductivity of gas mixtures*, Industrial & Engineering Chemistry, 42 (8), 1508-1511.

A Viscous drag

The phases motion is coupled through viscous drag forces. A Stokes drag type correlation is used. This force reads for one particle of constant radius R:

$$\mathbf{f}_{g\to p} = 6\pi\mu R(\mathbf{u} - \mathbf{u}_p), \tag{16}$$

with μ the gas viscosity. Let Re_p be the particle Reynolds number (based on the relative velocity between both phases) and C_d a drag coefficient depending on the flow regime [47].

$$Re_p = \frac{2R\rho\|\mathbf{u} - \mathbf{u}_p\|}{\mu},$$

$$C_d = \begin{cases} \dfrac{24}{Re_p}\left(1 + 0.15Re_p^{0.687}\right) & \text{if } Re_p < 800, \\ 0.438 & \text{otherwise.} \end{cases}$$

Using the volume fraction of the diluted phase, and the expression of the particle Reynolds number, the viscous drag force for a cloud of particles reads:

$$\mathbf{F}_{g\to p} = \frac{3\alpha_p C_d \rho\|\mathbf{u} - \mathbf{u}_p\|(\mathbf{u} - \mathbf{u}_p)}{8R}. \tag{17}$$

With,

$$\alpha_p = \frac{\rho_p}{\rho_c},$$

where ρ_p corresponds to the real density of the material constituting the particles, and ρ_p the apparent density of the particles.

B Heat exchange coefficient

In order to evaluate the exchange coefficient h, a correlation based on the Nusselt number is used,

$$Nu = \frac{hL}{\lambda} \Longrightarrow h = \frac{\lambda Nu}{L},$$

Where L is a characteristic length of the system and λ is the thermal conductivity. The Nusselt number is expressed with two dimensionless number, the Reynolds number and the Prandtl number. There exists many correlations of Nusselt number. These correlations depend on the flow configuration. In the present paper, we take the example of forced convection,

$$\begin{cases} Nu = 0.664Re^{1/2}Pr^{1/3} & \text{if Re} < 5.10^5, \\ Nu = 0.0365Re^{4/5}Pr^{1/3} & \text{otherwise.} \end{cases}$$

It is also possible to express a radiative heat flux (denoted by ϕ) using the Stefan law,

$$\phi = \epsilon\sigma S(T_{wall}^4 - T_i^4),$$

where, σ is the Stefan-Boltzmann constant and ϵ, the surface emissivity (depending on the material). It is possible to reduce this last expression when the difference between the wall temperature and the ambient temperature is weak,

$$\phi = 4\epsilon\sigma S T_a^3(T_{wall} - T_i),$$

where T_a corresponds to averaged temperature. Finally a radiative exchange coefficient can be expressed as follows,

$$h_r = 4\epsilon\sigma T_a^3.$$

Using all these considerations, the overall exchange coefficient is the following:

$$h_c = \frac{\lambda Nu}{L} + 4\epsilon\sigma T_a^3.$$